JGR Oceans

RESEARCH ARTICLE
10.1029/2022JC018939

Coaction of Top and Bottom Drags in Gulf Stream Dynamics

L. Renault[1], **P. Marchesiello**[1], **and M. Contreras**[1]

[1]LEGOS, University of Toulouse, IRD, CNRS, CNES, UPS, Toulouse, France

Key Points:

- Top and bottom friction affect the Gulf Stream dynamics in different ways but top drag reduces the model sensitivity to bottom friction
- A stress-correction approach for top drag is validated for Gulf Stream dynamics
- A scale-aware parameterization of subgrid topography gives encouraging results

Correspondence to:

L. Renault,
lionel.renault@ird.fr

Citation:

Renault, L., Marchesiello, P., & Contreras, M. (2023). Coaction of top and bottom drags in Gulf Stream dynamics. *Journal of Geophysical Research: Oceans*, *128*, e2022JC018939. https://doi.org/10.1029/2022JC018939

Received 7 JUN 2022
Accepted 13 FEB 2023

Author Contributions:

Conceptualization: L. Renault, P. Marchesiello
Formal analysis: L. Renault, P. Marchesiello
Funding acquisition: L. Renault
Investigation: L. Renault, P. Marchesiello, M. Contreras
Methodology: L. Renault, P. Marchesiello
Project Administration: L. Renault
Software: L. Renault
Supervision: L. Renault
Validation: L. Renault, P. Marchesiello
Visualization: L. Renault
Writing – original draft: L. Renault, P. Marchesiello, M. Contreras
Writing – review & editing: L. Renault, P. Marchesiello, M. Contreras

Abstract Bottom drag and top drag—associated with the ocean current feedback (CFB) to the atmosphere—are the energy dissipation processes in the oceanic boundary layers. Both are instrumental in regulating western boundary currents, such as the Gulf Stream (GS). However, the sensitivity of model results to bottom drag parameterization has not yet been considered in simulations where top drag is present. So far, in the absence of top drag, the bottom drag coefficient turns out to be a very sensitive parameter of ocean models. Here, we re-examine this sensitivity when both top and bottom drag are considered in eddy-rich ocean simulations of the North Atlantic basin. The top drag is addressed with a parameterization that considers the wind adjustment to CFB. In agreement with previous studies, we confirm that top drag has a large control on GS dynamics by reducing mesoscale activity. Next, we show that the energy sink due to bottom drag increases when top drag is neglected, but that this increase only partially compensates for the absence of top drag. As a result, the GS representation is too sensitive to bottom drag. Finally, we propose a simple scale-aware parameterization of the subgrid-scale topographic effect on bottom drag. Our results suggest that for a realistic representation of GS dynamics and energy pathways, top and bottom drags must be considered together. Future studies should include processes missing from this study, such as submesoscale dynamics and the surface gravity waves at the ocean-atmosphere interface.

Plain Language Summary The oceanic boundary layers dissipate energy via top drag (related to wind) and topographic/bottom drag. These two processes have been shown to play a key role in the regulation of western boundary currents, such as the Gulf Stream (GS). However, bottom drag has, until now, only been considered without top drag. In this case, the models show a fairly strong sensitivity to the bottom drop. In this study, we re-examine this sensitivity by considering both top and bottom drags in eddy-rich ocean simulations of the North Atlantic basin. In agreement with previous studies, we first confirm that top drag exerts a significant control on the GS dynamics by reducing eddy activity. Then, we show that neglecting top drag is only partially compensated by bottom drag, thus leaving a surplus of energy as well as an exacerbated sensitivity of the GS representation in models to bottom drag friction. Finally, we propose a simple, scale-aware parameterization of the subgrid-scale topographic effect on the bottom drag that allows for resolution-dependent, spatially distributed bottom friction coefficients. Our results suggest that for a realistic representation of GS dynamics and energy pathways, among other processes, top and bottom drags must be considered together and appropriately parameterized.

1. Introduction

The Gulf Stream (GS) is a Western Boundary Current (WBC) that plays a key role in the global ocean circulation and regulation of the Earth's climate. Linear Sverdrup theory predicts that the volume transport of WBCs varies with the intensity of basin-scale wind stress curl. However, observations and high-resolution simulations (Bryan et al., 1995, 2007; Chassignet & Marshall, 2008; Couvelard et al., 2008; Gula et al., 2015, 2016; Özgökmen & Chassignet, 2002; Renault, Molemaker, Gula, et al., 2016; Renault, Marchesiello, et al., 2019; Spall, 1996) suggest a more complex picture where eddies and topography exert a strong influence over a wide range of temporal and spatial scales. Yet, despite numerous international programs of observation and modeling, numerical models still poorly simulate important aspects of GS circulation, particularly the location of its separation from the coast (Chassignet et al., 2003; Schoonover et al., 2016; Thompson & Schmitz, 1989).

Modeling studies in the last two decades have clarified some key elements of GS dynamics. GS separation appears primarily dependent on the continental slope curvature (Debreu et al., 2022; Schoonover et al., 2017; Stern, 1998). The role of the counterflowing Deep Western Boundary Current has been suggested (Hurlburt & Hogan, 2008; Spall, 1996; Zhang & Vallis, 2007), but is now considered somewhat marginal (Schoonover et al., 2017). Mesoscale eddies are a more important player. They are integral to WBC systems through eddy-mean

flow interaction (McWilliams, 2008). A minimum spatial resolution of $\frac{1}{10}^\circ$ is a necessary but not sufficient condition for capturing the GS separation (Bryan et al., 2007; Chassignet & Marshall, 2008; Schoonover et al., 2017), although this minimum tends to be revised downwards (Chassignet & Xu, 2017). A mechanistic description of eddies interacting with topography has also emerged quite recently (Gula et al., 2015). The Charleston Bump, located between the Florida Strait and Cape Hatteras, appears as a key region characterized by a large isobath curvature. This curvature enhances the production of eddies (Gula et al., 2015; Xie et al., 2007), which are then advected by the GS and interact with it. On the other hand, Renault, Molemaker, Gula, et al. (2016) and Renault, Marchesiesello, et al. (2019) show that the intensity of mesoscale activity is reflected in that of the inverse kinetic energy cascade, and an excess of activity can lead to destabilization of the GS path, with an unrealistic bimodal separation near Cape Hatteras.

Therefore, in mesoscale-resolving ocean models, a sink of energy is needed to stabilize WBCs. Submesoscale processes may provide a direct route to dissipation (Gula et al., 2016), which would partly justify the use of high turbulent viscosity to control GS dynamics (Chassignet et al., 2003; Chassignet & Marshall, 2008; Chassignet & Xu, 2017; Schoonover et al., 2016). However, stabilization may also arise from mesoscale ocean-atmosphere coupling. Ma et al. (2016) suggest that thermal coupling may impact the Kuroshio extension, but a larger effect was reported for momentum coupling due to surface current feedback (noted CFB) (Bye, 1985; Dewar & Flierl, 1987; Duhaut & Straub, 2006; Renault, Molemaker, McWilliams, et al., 2016; Rooth & Xie, 1992)). Although generally weaker than surface winds, surface oceanic currents modify the interfacial shear stress within feedback loops that affect both the atmospheric and oceanic boundary layers. This process is relatively weak in coarse-resolution coupled models but gains surprising intensity in high-resolution models (Jullien et al., 2020; Oerder et al., 2016; Renault, Molemaker, McWilliams, et al., 2016; Renault, Molemaker, Gula, et al., 2016; Renault, McWilliams, Penven, 2017; Renault et al., 2018; Renault, Marchesiello, et al., 2019; Renault et al., 2020; Seo et al., 2016; Seo, 2017). Overall, from an oceanic point of view, CFB slows down the mean circulation and induces a large energy sink from mesoscale eddies to the atmosphere. This sink, called eddy killing, is responsible for damping mesoscale activity by about 30%. This process has been confirmed by satellite observations (Renault, McWilliams, & Masson, 2017). In the GS system, it attenuates the eddy-mean flow interaction, stabilizing the mean flow and thus correcting the usual biases of GS representation by uncoupled models, without requiring a large turbulent viscosity (Renault, Marchesiello, et al., 2019). Similar results are presented for other regions, such as the Gulf of Mexico (Larrañaga et al., 2022) and the western Mediterranean Sea (Renault, Arsouze, & Ballabrera-Poy, 2021). CFB causes an adjustment of the overlying wind: for example, a positive surface current anomaly causes a positive 10-m wind anomaly. This wind adjustment must be parameterized in a forced ocean model to avoid overestimating the eddy killing effect (Renault, Molemaker, Mcwilliams, et al., 2016; Renault et al., 2020).

The CFB process is equivalent to a "top drag" (Dewar & Flierl, 1987) as it provides energy dissipation through friction at the top boundary of the ocean. In this sense, it works similarly to a bottom drag, which is another process affecting energy pathways in ocean models (Arbic et al., 2009; Sen et al., 2008; Trossman et al., 2017). Bottom drag is a complex process caused by either skin friction or flows separation over random topography, but it is often reduced in the bottom stress formulation to a constant drag coefficient C_d or roughness length z_{0b}. At resolutions of $\mathcal{O}$(10 km), bottom drag may be dominated by the effects of subgrid topography, called form drag. Form drag is associated with pressure gradients resulting from flow interaction with unresolved topography (Belcher & Wood, 1996), or with wave drag resulting from lee-wave breaking (Klymak, 2018; Trossman et al., 2013, 2016). The generation of lee-waves by the Gulf Stream interaction with small-scale topography was recently investigated by de Marez et al. (2020) using satellite sun glitter images and a high-resolution setting of the Coastal and Regional Ocean COmmunity model (CROCO). The study points again to the Charleston Bump as a hot spot of lee wave generation at length scales of 1–10 km and suggests enhanced local drag as a result. Parametrizations of form and wave drag due to subgrid topography were first implemented in atmospheric models to improve numerical weather predictions (Belcher & Wood, 1996; Jimenez & Dudhia, 2012) and were more recently applied to oceanic models (Trossman et al., 2013, 2016). Parametrizations generally rely on some measure of subgrid bathymetric variability, flow magnitude (or Froude number), and stratification. They enter the momentum equations through bottom stress, either as an effective roughness length or drag coefficient. However, most often, a constant standard value of $C_d = 1\text{–}5\ 10^{-3}$ or $z_{0b} = 0.1\text{–}1$ cm—larger than sand-grain roughness—is still used without much consideration for its physical meaning but relying on sensitivity evaluations.

Table 1
Sensitivity Experiments

Experiments	Current feedback	Z_{0b} [m]	Subgrid Topo
CFB_{Z1}	Parametrized	10^{-1}	None
CFB_{Z2}	Parametrized	10^{-2}	None
CFB_{Z3}	Parametrized	10^{-3}	None
CFB_{Z4}	Parametrized	10^{-4}	None
$NOCFB_{Z1}$	None	10^{-1}	None
$NOCFB_{Z2}$	None	10^{-2}	None
$NOCFB_{Z3}$	None	10^{-3}	None
$NOCFB_{Z4}$	None	10^{-4}	None
CFB_{Z3TOPO}	Parametrized	10^{-3}	Yes

Drag coefficients are sensitive parameters in oceanic models, since bottom drag—as top drag—produces a sink of energy for the GS, dissipating mean and mesoscale eddy flows (de Marez et al., 2020; Trossman et al., 2016). However, the sensitivity of oceanic models to bottom drag has, as yet, only been considered without top drag that results from ocean-atmosphere coupling. We will show in this paper that the top drag can mediate the impact of the bottom drag, reducing model sensitivity to drag coefficients. In uncoupled models, part of the energy that should be transferred to the atmosphere by CFB may be dissipated instead by bottom drag. In this sense, it may in some ways partially replace the top drag effect and help in the representation of some key features of GS, but for spurious reasons and with uncontrolled effects.

In the present study, we investigate the relation between top and bottom drag acting on the dynamics of the North Atlantic (NATL) basin. We will focus on the GS with a set of realistic, high-resolution simulations, including a simple parametrization of subgrid-scale topographic drag. The paper is organized as follows: model configuration and methodology are described in Section 2. In Section 3, the impact of top drag on GS and NATL circulations is revisited using the CFB parametrization proposed by Renault, Mcwilliams & Masson (2017) and Renault et al. (2020). In Section 4, the effect of bottom drag on GS and NATL circulations is also assessed, including the extent to which drag interacts with this effect. To this end, two sets of four simulations are carried out where CFB is accounted for or ignored and where bottom roughness length z_{0b} covers a large range of acceptable values from 10^{-4} to 10^{-1} m (see Table 1). Finally, a parametrization of bottom form drag is proposed and tested in Section 5. The results are discussed in Section 6, followed by conclusion.

2. Model Configuration and Methodology

2.1. Coastal and Regional Ocean COmmunity Model (CROCO)

The oceanic simulations are performed with the Coastal and Regional Ocean Community model (Debreu et al., 2012; Shchepetkin & McWilliams, 2005). CROCO is a free-surface, terrain-following coordinate model with split-explicit time stepping and with Boussinesq and hydrostatic approximations (a non-hydrostatic solver is also available but not needed at mesoscale resolution). A third-order predictor-corrector time step algorithm and high-order numerical discretization of pressure gradients and momentum advection reduce numerical dispersion and diffusion to achieve an effective resolution of 5–10 times the horizontal resolution (Soufflet et al., 2016). For tracers, a third-order upstream biased advection scheme is split and its diffusion part is rotated along the isopycnal surfaces to avoid excessive diapycnal mixing (Lemarié et al., 2012; Marchesiello et al., 2009). A nonlocal planetary K-profile boundary layer scheme (Large et al., 1994) parameterizes unresolved turbulent diffusion at the surface, bottom, and interior of the ocean.

The NATL domain is identical to that presented in Renault, Molemaker, Gula, et al. (2016). It has a horizontal spatial resolution of 6–7 km, with 1152 × 1059 grid points. The grid encompasses the full North Atlantic Gyre and Subpolar Gyre, extending from 133.7°W to 21.7°W and from 0.4°N to 73.2°N. The bathymetry is constructed from the Shuttle Radar Topography Mission (SRTM30 plus) dataset based on the 1-min Sandwell and Smith (1997) global dataset and higher-resolution data where available. To avoid aliasing whenever the topographic data are available at a higher resolution than the computational grid and to ensure the smoothness of topography at the grid scale, a Gaussian smoothing kernel with width four times the topographic grid spacing is used. Pressure gradient errors caused by terrain-following coordinates are avoided by a specifically designed numerical scheme (Shchepetkin & McWilliams, 2003) and by applying local smoothing of the bottom topography where its slope exceeds an r-factor value of 0.2. We use 50 σ levels in the vertical (Shchepetkin & McWilliams, 2009) with stretching parameters that are set to increase the resolution near the surface and the bottom with parameters $\theta_s = 7$ and $\theta_b = 2$. We also set $h_{cline} = 300$ m, controlling the transition depth between the flat z-levels and the terrain-following σ levels, to mitigate σ errors from the pressure gradient and advection terms in the pycnocline. σ errors associated with lateral tracer advection are more generally addressed by removing spurious diapycnal diffusion induced by the upstream advection scheme (Lemarié et al., 2012; Marchesiello et al., 2009). As in Renault, Molemaker, Gula, et al. (2016), the numerical solution is first spun up for 14 years

using climatological monthly surface fluxes and initial and lateral oceanic boundary conditions from a climatological state of the Simple Ocean Data Assimilation (SODA; Carton & Giese, 2008) representing Jan. 1st. The simulation is then run for an additional 6 years, from 2010 to 2016, using interannual surface forcing derived from the hourly Climate Forecast System Reanalysis V2 (CFSRV2, Saha et al. (2010)). The Bulk parametrization from Fairall et al. (2003) is used to estimate freshwater, heat, and momentum turbulent fluxes. Note that the CFSRV2 winds are corrected using the mean monthly climatology from a WRF simulation over the North Atlantic region (Renault, Molemaker, Gula, et al., 2016), making the simulations comparable to those of Renault, Molemaker, Gula, et al. (2016). At oceanic open boundaries, data of temperature, salinity, surface elevation, and horizontal velocities are taken from interannual, monthly-averaged SODA outputs with a spatial grid resolution of 1/4°× 1/4°(Carton & Giese, 2008). The boundary condition algorithm consists of an active-passive 2D radiation scheme for the baroclinic mode (including T and S) and a modified Flather-type scheme for the barotropic mode (Marchesiello et al., 2001).

2.1.1. Bottom Drag Parametrization

Bottom drag is computed assuming that the flow in the bottom boundary layer has a classic vertical logarithmic profile, defined by a friction velocity u_* and a bottom roughness length Z_{0b} (m):

$$|\mathbf{u}_b| = \sqrt{u_b^2 + v_b^2} = \frac{u_*}{\kappa} \log \frac{z_b}{Z_{0b}}, \tag{1}$$

where log is the natural logarithm, u_b and v_b are the oceanic near-bottom currents in the log layer at a height z_b above bed (here corresponding to the first vertical grid level); $u_* = \sqrt{\tau_b}$ with τ_b the bottom stress; $\kappa = 0.41$ the von Karman constant; Z_{0b}, the bottom roughness length, is given constant values of 10^{-4}, 10^{-3}, 10^{-2}, or 10^{-1} m (Table 1). The zonal and meridional components of bottom stress are then calculated as:

$$\left[\tau_{bx}, \tau_{by}\right] = C_{db} \, |\mathbf{u}_b| \, [u_b, v_b], \tag{2}$$

with the drag coefficient:

$$C_{db} = \frac{\kappa^2}{\log^2 \frac{z_b}{Z_{0b}}} \tag{3}$$

2.1.2. Top Drag Parametrization

When CFB is considered in a coupled Ocean-Atmosphere model, the surface stress is estimated using the following equation in both the bulk formulae and the tridiagonal matrix system solved in the vertical turbulent diffusion scheme (Lemarié, 2015; Renault, Lemarié, & Arsouze, 2019):

$$\boldsymbol{\tau} = \rho_a C_D (\boldsymbol{U_a} - \boldsymbol{U_o}) |\boldsymbol{U_a} - \boldsymbol{U_o}| \tag{4}$$

Where C_D is the surface drag coefficient estimated using the Fairall et al. (2003) bulk parameterization. When CFB is ignored, the same equation applies but with $\boldsymbol{U_o} = 0$.

CFB induces wind anomalies that cause a partial re-energization of the ocean (Renault, Molemaker, Mcwilliams, et al., 2016), that is, negative feedback from the atmosphere to the ocean. Therefore, in a forced ocean model, the use of Equation 4 removes the negative feedback and causes an overestimation of the CFB effect and in particular a too-strong eddy killing. A CFB parameterization that mimics the associated wind response and, thus, allows for partial re-energization of the ocean by winds is therefore required. To this end, Renault, Mcwilliams &Masson (2017) and Renault et al. (2020) suggest using a stress correction approach, which is based on the current-stress coupling coefficient s_τ. It mimics the coupled surface stress response that includes the wind adjustment:

$$\boldsymbol{\tau} = \boldsymbol{\tau_0} + \boldsymbol{\tau}', \tag{5}$$

where $\boldsymbol{\tau}$ is the surface stress that includes the CFB effect; $\boldsymbol{\tau_0}$ is the surface stress that does not include the CFB effect and is estimated using absolute winds and drag coefficients from bulk parametrization (including stability functions); and $\boldsymbol{\tau}'$ is the surface stress response to an oceanic current $\boldsymbol{U_o}$:

$$\boldsymbol{\tau}' = s_\tau \boldsymbol{U_o}. \tag{6}$$

s_τ is predicted statistically based on the wind magnitude at 10 m (U_{10}), following Renault, Mcwilliams & Masson (2017), and Renault et al. (2020)):

$$s_\tau = \alpha U_{10} + \beta, \tag{7}$$

with $\alpha = -2.9 \times 10^{-3}$ N s^2 m^{-4}, and $\beta = 0.008$ N s m^{-3}. For weak winds (<3 ms^{-1}), s_τ keeps the value of -0.0007 N s m^{-3} given for 3 ms^{-1} winds.

2.2. Experimental Design

Two sets of four simulations were performed over a 6-year period, from 2011 to 2016, discarding the first year, which was used for spin up (Table 1). A first set of simulations is performed with top drag, using z_{0b} equal to 10^{-4} , 10^{-3} , 10^{-2} , and 10^{-1} , namely CFB$_{Z4}$, CFB$_{Z3}$, CFB$_{Z2}$, and CFB$_{Z1}$, respectively. For a second set of simulations, the CFB is ignored using the surface stress $\boldsymbol{\tau_0}$ calculated from the absolute wind with a bulk formula (Fairall et al., 2003). As with the CFB simulations, the NOCFB simulations NOCFB$_{Z4}$, NOCFB$_{Z3}$, NOCFB$_{Z2}$, and NOCFB$_{Z1}$ differ in the value of z_{0b}.

2.2.1. A Parametrization of Bottom Form Drag

In the present formulation, we do not differentiate between form drag and wave drag processes and between steady and oscillating flow conditions (Klymak, 2018; Trossman et al., 2016), but rather introduced a simple way to impose a momentum sink associated with the unresolved topography. We drew on the work of Jimenez and Dudhia (2012) for the WRF model and used the same modulation of a quadratic bottom drag by a coefficient dependent on topographic roughness at the subgrid scale. This rather basic approach takes a step forward from the usual constant roughness length (of 1 cm, typically used in ROMS and CROCO applications) to allow for scale-dependent roughness heterogeneity with a controllable parameter.

Following Jimenez and Dudhia (2012)—who attempted to correct a high wind speed bias in WRF—we associate the bottom form drag with the magnitude of subgrid-scale topographic variability. The effects of the unresolved terrain are parametrized with a correction factor c_t that modulates the frictional drag τ_b in the momentum equations (the bottom stress is simply multiplied by c_t). c_t is formulated as the logarithmic function of subgrid-scale topographic variance σ_t multiplied by a corrective factor α_c (Jimenez & Dudhia, 2012):

$$c_t = \max(1, \alpha_c \log(\sigma_t)) \tag{8}$$

Here $\alpha_c = 0.8$. The variance of unresolved topography given by SRTM30 corresponds to wavelengths of 1–10 km, which coincides with the relevant scales of wave drag due to lee waves (de Marez et al., 2020). We assume here, for simplicity, that Froude number and stratification are everywhere favorable to the generation and breaking of lee waves within this range of unresolved topographic variability. This can obviously be further improved (Trossman et al., 2016), but is adapted to our present objective, which is to document the sensitivity of GS dynamics to a spatially heterogeneous distribution of topographic roughness. It is also a first step in setting a resolution-dependent roughness (through σ_t) for future investigation at higher resolution, where the drag coefficient should be reduced. For the present test, the simulation CFB$_{Z3TOPO}$ is similar to CFB$_{Z3}$, with the modulation of τ_b by c_t (see also Table 1).

2.3. Diagnostic Methods

All quantities follow a Reynolds decomposition into a seasonal mean over the 2011–2016 period and are indicated with an overbar ($-$) and its deviations noted by primes (').

2.3.1. Energy Conversion

Considering that wind forcing of ageostrophic motions does not feed directly into the general circulation (Renault, McWilliams, et al., 2021; Scott & Xu, 2009; von Storch et al., 2007; Wunsch, 1998), we focus on the following relevant source and eddy-mean conversion terms (Marchesiello et al., 2003; Stern, 1975).

- The mean geostrophic wind stress work:

$$F_m K_{mg} = \frac{1}{\rho_0} \left(\overline{\tau_x}\, \overline{u_{og}} + \overline{\tau_y}\, \overline{v_{og}} \right), \tag{9}$$

where u_{og} and v_{og} are the surface geostrophic zonal and meridional velocities.

- The eddy geostrophic wind stress work:

$$F_e K_{eg} = \frac{1}{\rho_0}\left(\overline{\tau'_x u'_{og}} + \overline{\tau'_y v'_{og}}\right). \tag{10}$$

- The mean bottom stress work:

$$BF_m K_m = \frac{1}{\rho_0}\left(\overline{\tau_{bx}}\,\overline{u_b} + \overline{\tau_{by}}\,\overline{v_b}\right), \tag{11}$$

where τ_{bx} and τ_{by} are the bottom zonal and meridional stress and u_b and v_b are the bottom zonal and meridional velocities (presented above).

- The eddy bottom stress work:

$$BF_e K_e = \frac{1}{\rho_0}\left(\overline{\tau'_{bx} u'_b} + \overline{\tau'_{by} v'_b}\right). \tag{12}$$

$F_m K_{mg}$ represents the energy transfer from the mean surface wind forcing to the mean kinetic energy, $F_e K_{eg}$ is the energy transfer from the surface wind forcing anomalies to the geostrophic EKE.

2.3.2. Barotropic Vorticity Budget

Oceanic gyre circulation can be approached by the barotropic vorticity budget, which is an extension of the Sverdrup balance. Following, for example, Couvelard et al. (2008); Schoonover et al. (2016), the barotropic vorticity budget is computed by taking the rotational of the vertically integrated lateral momentum equations:

$$\frac{\partial \overline{\zeta}}{\partial t} = \frac{J(P_b, h)}{\rho_0} - \mathcal{A} - \nabla.(f\mathbf{U}) + \frac{\nabla \times \tau}{\rho_0} - \frac{\nabla \times \tau_\mathbf{b}}{\rho_0} + \mathcal{D}, \tag{13}$$

where $\partial\overline{\zeta} = (\nabla \times \mathbf{U}).\hat{z}$ is the barotropic vorticity; $\mathbf{U}$ the barotropic current; J the Jacobian operator, P_b the bottom pressure; h the bathymetry; $\mathcal{A}$ the nonlinear torque (vorticity advection); f the Coriolis force; τ and $\tau_\mathbf{b}$ the surface and bottom stress vectors respectively; and $\mathcal{D}$ the viscous torque. In the following, the right-hand-side terms of Equation 13 are referred to as bottom pressure torque $\left(\frac{J(P_b,h)}{\rho_0}\right)$, nonlinear torque ($\mathcal{A}$), planetary vorticity advection ($-\nabla.(f\mathbf{U})$), wind stress curl $\left(\frac{\nabla\times\tau}{\rho_0}\right)$, bottom stress curl $\left(-\frac{\nabla\times\tau_\mathbf{b}}{\rho_0}\right)$ and viscous torque ($\mathcal{D}$).

The bottom pressure torque is a measure of the topographic steering of the flow (Couvelard et al., 2008). The nonlinear torque represents the advection of vorticity by the mean and eddy flow. The planetary vorticity advection is due to the combined effects of the earth's curvature and rotation (β term in the Sverdrup balance). The surface stress curl is a top drag curl and can be both a source or dissipation of vorticity. The bottom stress curl is the drag effect of unresolved topography. Finally, the viscous torque represents the vorticity dissipation due to turbulent viscosity. In a regional simulation, it has large values only within sponge layers near the open boundaries.

3. Top Drag Effect on Ocean Dynamics

The modulation of GS dynamics by CFB (top drag) was demonstrated by Renault, Molemaker, Gula, et al. (2016) and Renault, Marchesiello, et al. (2019) using ocean-atmosphere coupled simulations and a roughness $Z_{0b} = 1\ cm$. Here, we revisit this coupling effect using forced simulations that use the same Z_{0b} value and that may or may not include a CFB parameterization on the surface stress. (CFB_{Z2} or $NOCFB_{Z2}$; Section 2.1.2).

3.1. Mean Circulation

Figure 1 shows the mean dynamic topography from the CNES/AVISO2018 product and CFB_{Z2}. The mean dynamic topography is well reproduced by CFB_{Z2}. In particular, the simulated GS path is highlighted by the zero SSH contour in Figure 1, shows very good agreement with the observations.

To further assess the realism of the simulations and CFB effects on the GS, mean geostrophic surface currents from CFB_{Z2} and $NOCFB_{Z2}$ are compared in Fig. 2ab with the equivalent field derived from AVISO mean dynamic

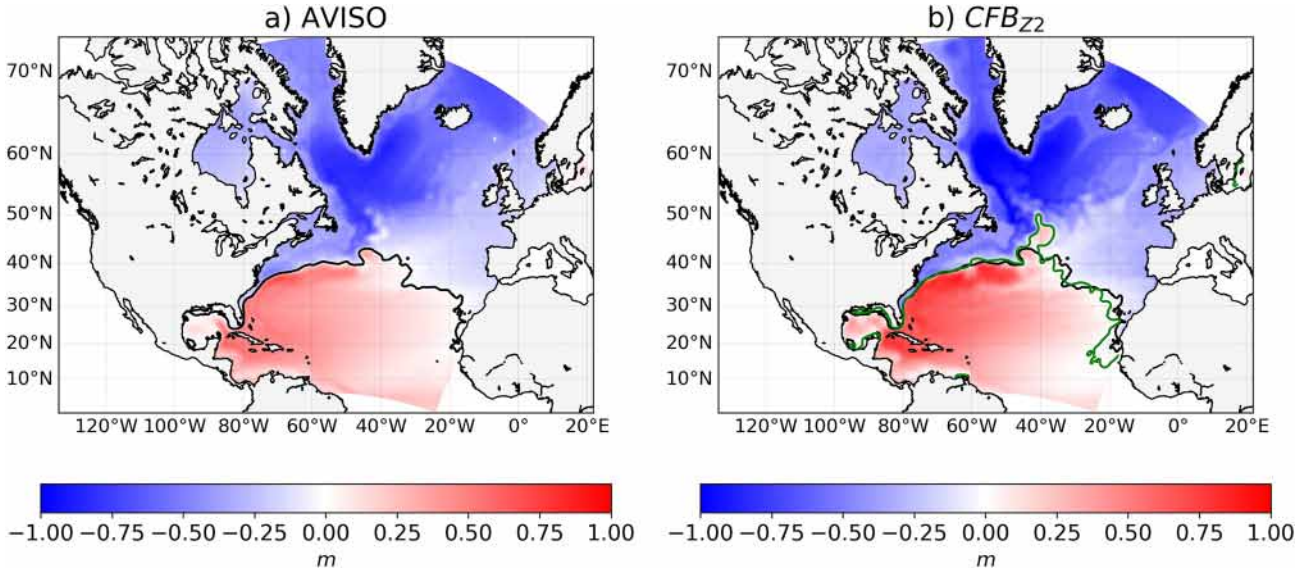

Figure 1. Mean Dynamic Topography (m.) from (a) the CNES/AVISO2018 product and (b) CFB_{Z2}. The Gulf Stream path is highlighted with the black and green lines that represent the contour of 0 m from AVISO and CFB_{Z2}, respectively.

topography (Rio et al., 2014). The red and black contours represent the mean path of the GS identified using the contour of 0.6 ms^{-1} from the simulations and the AVISO mean dynamic topography, respectively. The two solutions appear similar over the Charleston Bump, but the GS separation is largely impacted by CFB, consistently with Renault, Molemaker, Gula, et al. (2016). In $NOCFB_{Z2}$, the GS separates downstream of the observed location at Cape Hatteras. CFB improves the GS pathway and, in particular, its separation near Cape Hatteras by weakening the mean flow by ≈12%, either directly or, more importantly, through eddy damping and subsequent weakening of the inverse cascade of kinetic energy (Renault, Molemaker, Gula, et al., 2016; Renault, Marchesiello, et al., 2019). Figure 2c shows alongstream GS transports. Consistent with Renault, Molemaker, Gula, et al. (2016), the GS transport post-separation is weaker in CFB_{Z2} than $NOCFB_{Z2}$ by ≈15%. The most striking difference between the simulations occurs between Cape Hatteras and the New England Seamount, where $NOCFB_{Z2}$ shows excessive transport compared with observations by Johns et al. (1995), while CFB_{Z2} is more realistic with ≈120 Sv.

To better characterize the position of the GS separation, the monthly position of the GS separation is derived via a sea surface height (SSH) contour and tracked through the daily fields from AVISO and from the simulations. Similarly to Schoonover et al. (2017), the contour value is determined from SSH at 28°N where the surface Gulf Stream speed is at 80% of its maximum. The GS separation latitude is computed following this contour and averaging its latitude between 74.6°W and 74.4°W. Figures 3a and 3b illustrate a separation position from CFB_{Z2} and $NOCFB_{Z4}$ and Figure 3c a boxplot of the position of the GS separation from AVISO and the simulations. In AVISO, the position of the GS separation is relatively stable with a mean and median separation at ≈ 35.7°N. The length of the box shows the upper and lower quartiles whereas the extreme lines represent the 5th and 95th percentiles of the distributions. In AVISO, the position of the GS separation has a variation of <1°. In $NOCFB_{Z2}$, the GS separates prematurely with a mean position around 35.0°N and has too large a variability, indicating excess meandering. Consistent with Figure 2, CFB improves the GS pathway in CFB_{Z2}—and, in particular, its separation near Cape Hatteras (mean position around 35.8°N). Finally, the GS separation in CFB_{Z2} is very similar to that in the coupled simulation of Renault, Molemaker, Gula, et al. (2016). Both coupled and forced simulations to share a similar configuration with the same bottom drag parameterization. Furthermore, in the forced simulation, the winds are corrected using the average monthly climatology derived from the coupled simulation. Therefore, while we do not expect a match of the two solutions at each moment in time, the statistical similarity between the two simulations over the 5-year period holds as a validation of the CFB parameterization.

The realism and sensitivity of the GS to CFB can be further assessed by analyzing the vertical flow structure near Cape Hatteras. Figure 4 shows a cross-section of geostrophic currents from near Cape Hatteras, as made by Pickart and Smethie (1993) from in situ observations during summer (see their figure 3). In agreement with

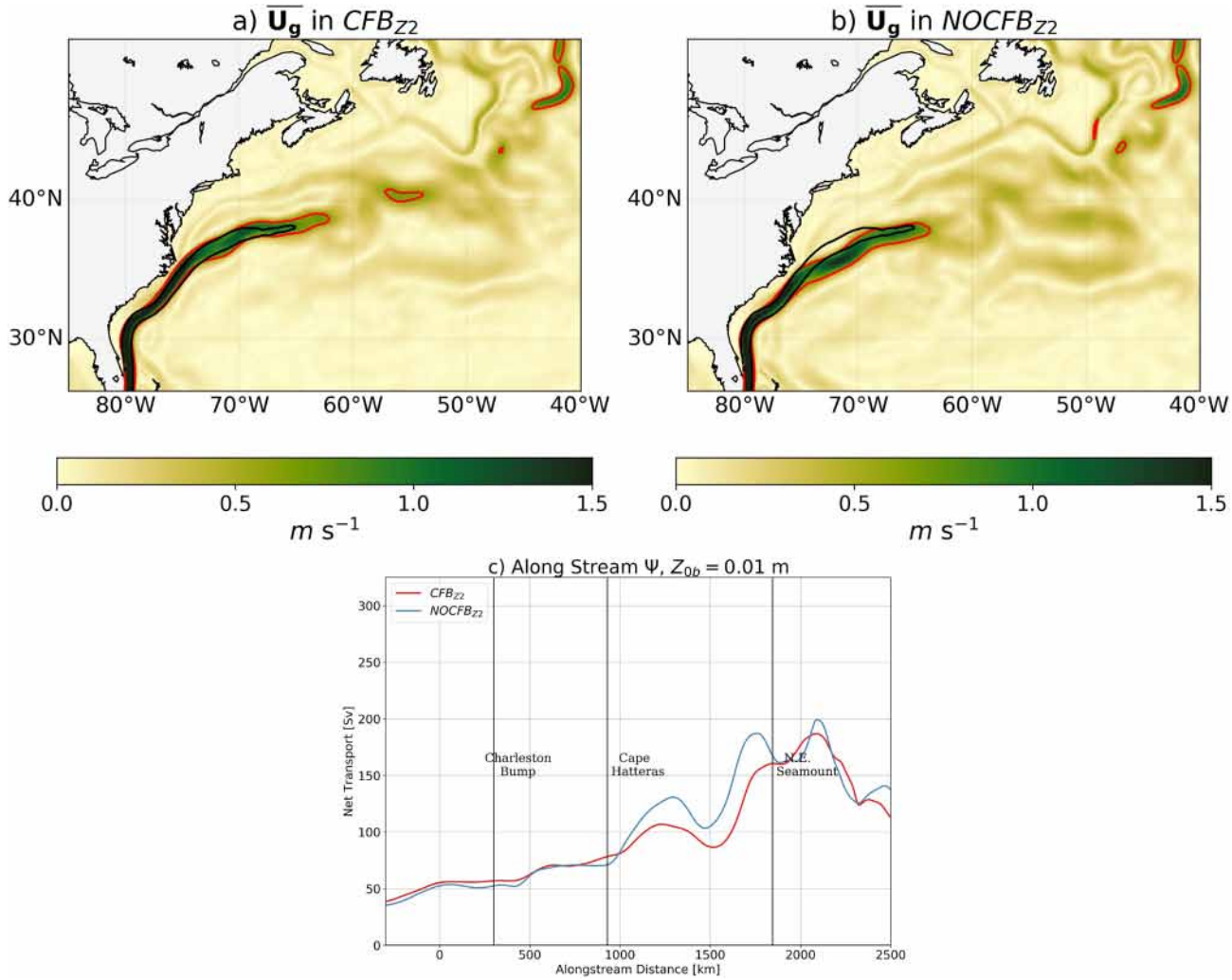

Figure 2. Mean surface geostrophic currents from CFB_{Z2} (a) and $NOCFB_{Z2}$ (b) simulations zoomed over the Gulf Stream. The red and black contours represent the mean path of the Gulf Stream identified using the contour of 0.6 m s^{-1} from the simulations and from the AVISO MDT, respectively. (c) Alongstream GS transport estimated from CFB_{Z2} (red) and $NOCFB_{Z2}$ (blue).

Pickart and Smethie (1993), in CFB_{Z2}, the mean velocity section at Cape Hatteras reveals that the GS is concentrated in the first 1,000 m of depth, with a core in the first 100 m and velocities greater than 1.5 m s^{-1}. By contrast, in $NOCFB_{Z2}$ the GS extends too far offshore, which is consistent with a premature GS separation in Figure 3c.

3.2. Mesoscale Activity

As a measure of mesoscale activity, surface geostrophic EKE is computed from daily geostrophic surface current perturbations in CFB_{Z2} and $NOCFB_{Z2}$ and compared with that estimated from AVISO (Figure 5a-c). AVISO is only able to resolve eddies with a radius longer than about 40 km and a lifetime longer than a week (Chelton et al., 2011). Therefore, to ensure a fair model-data comparison, we use a 7-day time averaging and a spatial Gaussian filter with a cutoff of ≈50 km. In agreement with previous studies, EKE in $NOCFB_{Z2}$ is larger than observed over the Caribbean Sea, the Gulf of Mexico (not shown), and along the GS path. In CFB_{Z2}, the surface and depth-integrated EKE are reduced by 32% and 30% respectively over the whole domain. Figure 5d depicts the integrated EKE over the GS separation region (black box in Figure 5a) and post-separation region (red box in Figure 5a). The integrated EKE in CFB_{Z2} is in very good agreement with AVISO in both regions, while the values are clearly overestimated in $NOCFB_{Z2}$, especially in the post-separation region. The loss of energy in CFB_{Z2} is explained by the eddy wind work F_eK_{eg} (Equation 10) shown in Figure 6, a process called

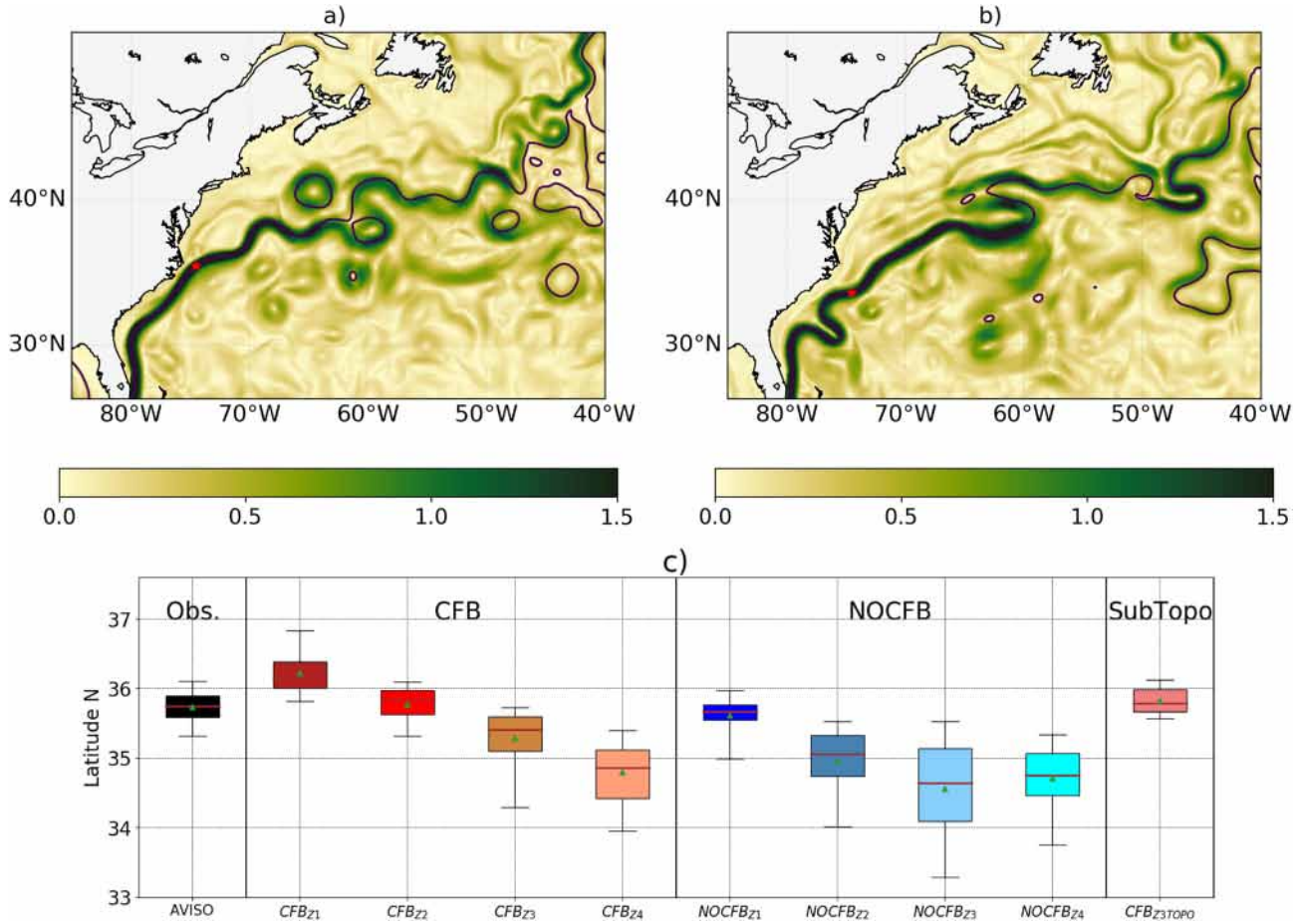

Figure 3. Illustration of Gulf Stream (GS) separation from CFB_{Z2} (a) and $NOCFB_{Z4}$ (b) estimated by the detection method. The colors represent the mean surface geostrophic currents; the thick black outline highlights the current detected path and the red star the GS separation position (see text for more details). (c) Box plots of monthly temporal variability of GS position from AVISO and simulations. The green dot represents the mean of the data, whereas the line that divides the box into two parts represents its median. The length of the box indicates the upper and lower quartiles and the extreme lines, the 5th and 95th percentiles of the distributions. Statistical significance of the medians and means shown in the box plots have been tested with a bootstrap method. For all the box plots depicted here and in the following figures, the 95% confidence intervals of the means and medians are indistinguishable from the symbol used.

eddy killing that extracts energy from mesoscale currents to the atmosphere. This energy sink stabilizes the mean GS flow via a reduced inverse cascade Renault, Marchesiello, et al. (2019), and thus improves the realism of GS separation.

In the GS post-separation region, the deep oceanic variability is mainly controlled by surface currents via vortex stretching (Chassignet & Xu, 2017). Thoppil et al. (2011) show that a realistic representation of upper-ocean EKE is critical for abyssal circulation. Therefore, the top drag caused by CFB is likely to affect the abyssal circulation as well. Following Chassignet and Xu (2017), we present vertical sections of mean zonal flow and EKE along 55°W from CFB_{Z2} and $NOCFB_{Z2}$ (Figure 7), which can be compared with long-term observations of the POLYMODE experiment (Richardson, 1985; figure 3ab). Here, EKE is estimated using total currents. Again, the mean and eddy flow of the GS in $NOCFB_{Z2}$ extends too far offshore, compared with a sharper and stronger current in CFB_{Z2}. In $NOCFB_{Z2}$, this leads to an excess in the vertical redistribution of energy, which feeds the mean abyssal circulation (10 cm s^{-1} in $NOCFB_{Z2}$ at depth vs. 5 cm s^{-1} in CFB_{Z2}), and to an overly barotropic GS in the post-separation region. CFB thus improves the realism of the abyssal circulation by reducing both the mean and eddy flow at depth. This is in agreement with Thoppil et al. (2011) and Chassignet and Xu (2017) who suggest that the coupling between surface and abyssal circulation is controlled by barotropization and inverse energy cascade.

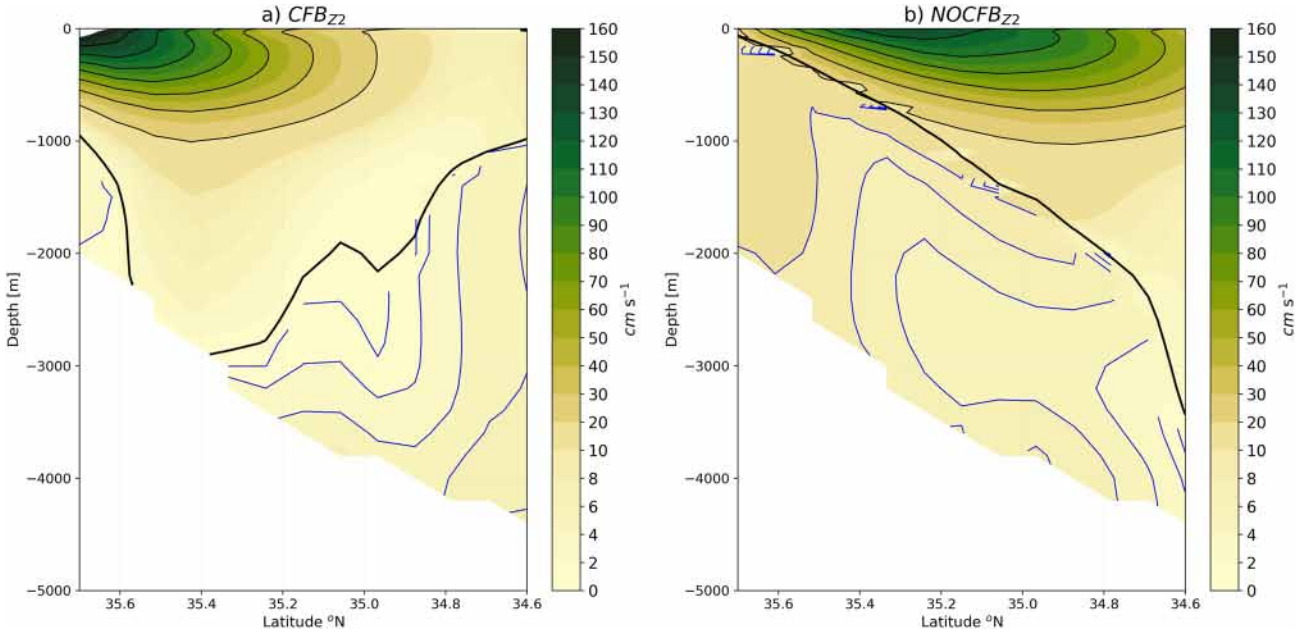

Figure 4. Cross-section at Cape Hatteras of the mean geostrophic current during summer from CFB_{Z2} (a) and $NOCFB_{Z2}$ (b).

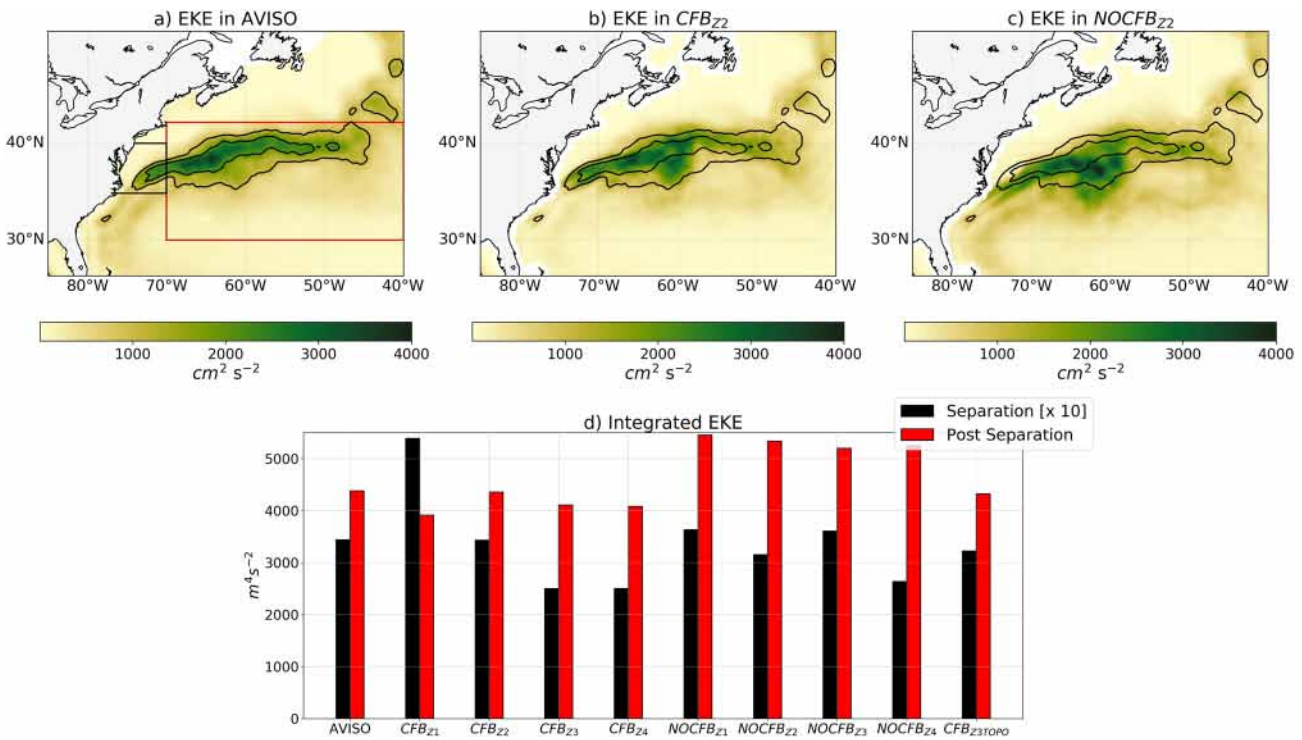

Figure 5. Top panel: Mean surface geostrophic EKE estimated from AVISO (a), CFB_{Z2} (b), and $NOCFB_{Z2}$ (c). The contours represent the EKE levels of both 1,000 and 2,000 $cm^2\ s^{-2}$ from AVISO. A 7-day time averaging and a spatial Gaussian filter with a cutoff of ≈50 km is applied on the simulated SSH to mimic AVISO. Bottom panel: Spatially integrated surface geostrophic EKE from AVISO and the simulations over a Gulf Stream separation region (black box in (a)) and a post-separation region (red box in (a)).

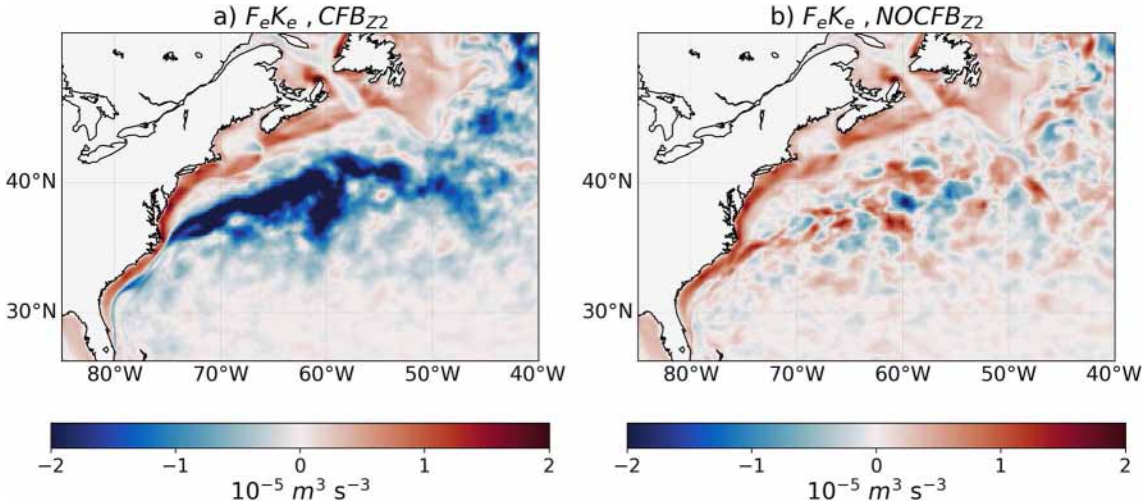

Figure 6. Dissipation of energy at mesoscale currents induced by F_eK_e from CFB_{Z2} (a) and $NOCFB_{Z2}$ (b).

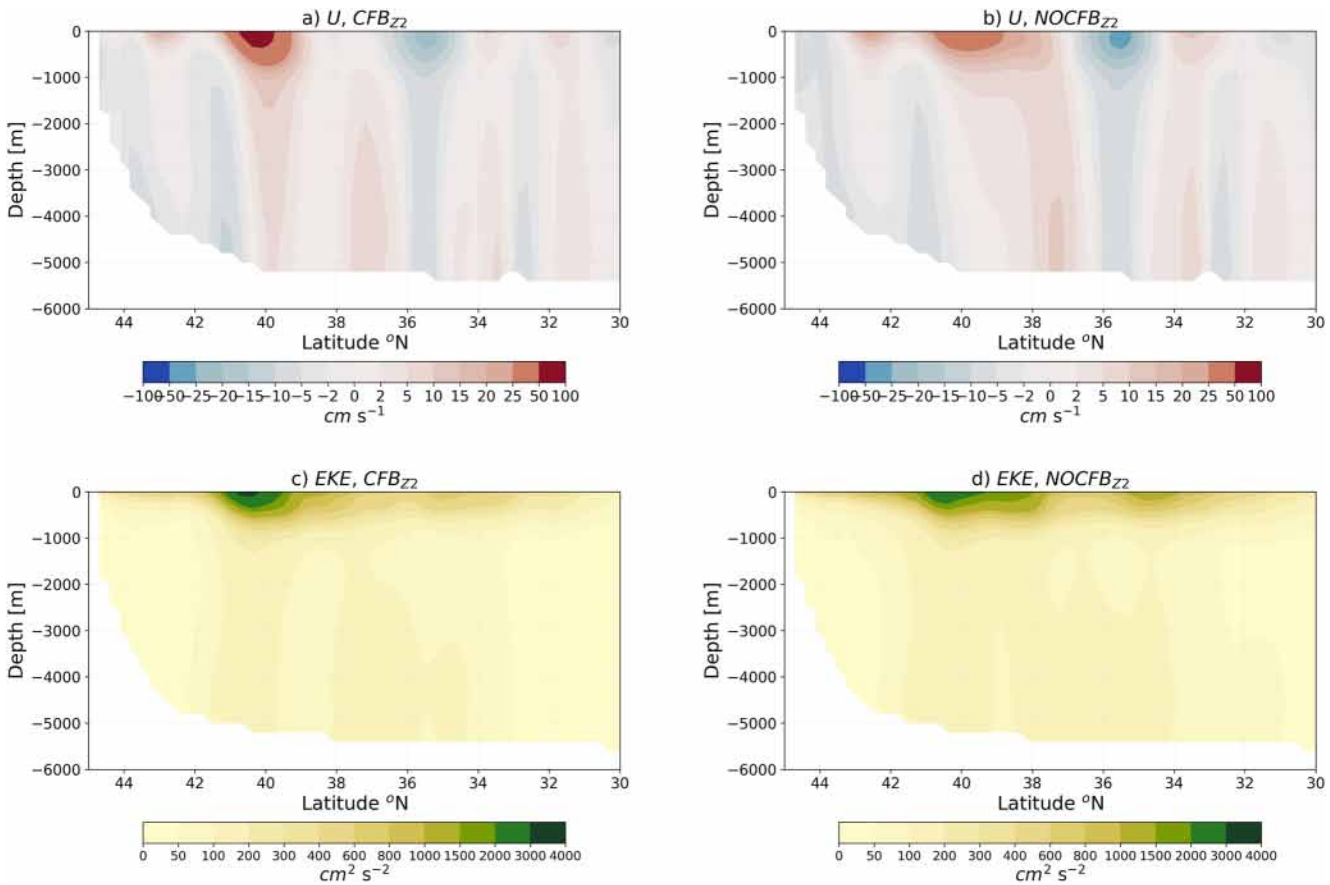

Figure 7. Vertical distribution of zonal velocity and EKE along 55°W from CFB_{Z2} (a)–(c) and $NOCFB_{Z2}$ (b)–(d). The reduction of the mean and eddy surface circulation by current feedback also induces a weakening of the abyssal circulation.

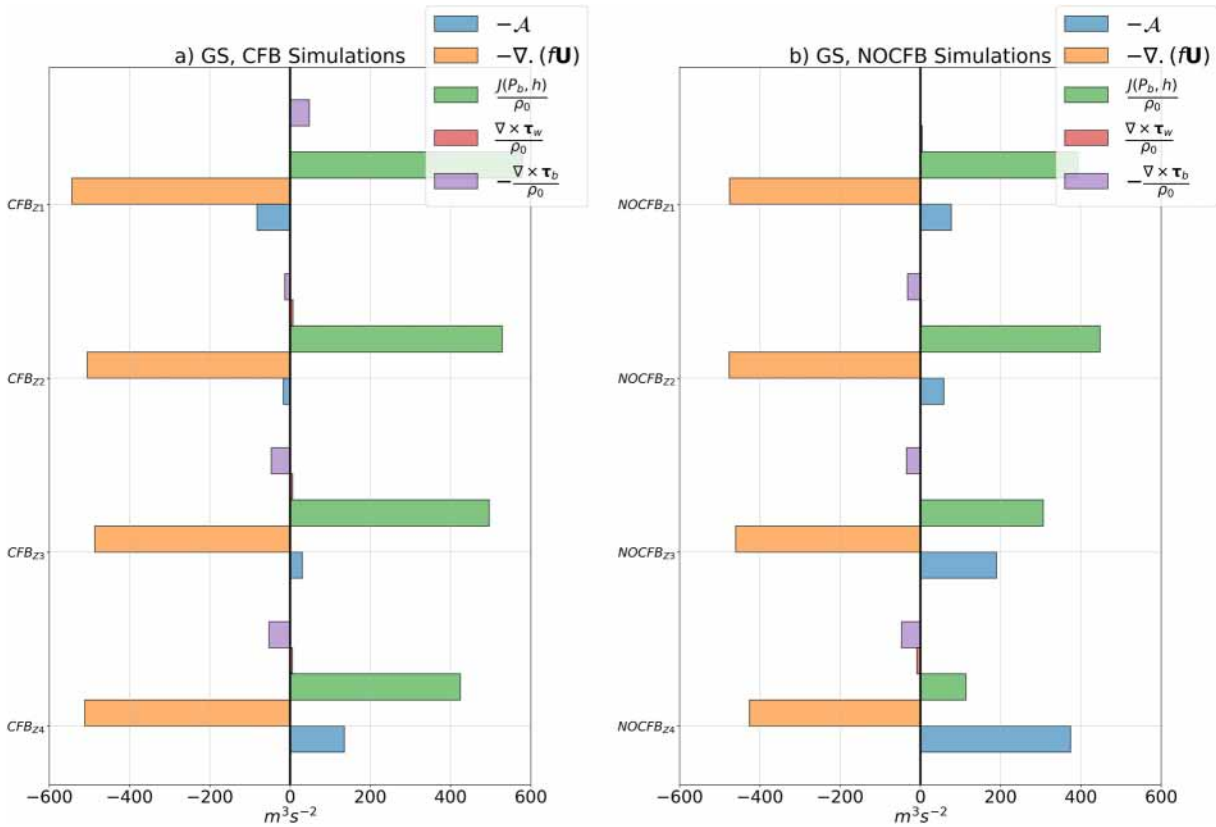

Figure 8. Time-averaged of the barotropic vorticity budget for the Gulf Stream from the current feedback simulations (a) and the NOCFB simulations (b).

4. Bottom Drag Effect on Ocean Dynamics

4.1. Vorticity and EKE Budgets

In this section, we assess the role of bottom drag in driving GS and NATL circulations, when associated with top drag (from CFB). To this end, we analyze simulations CFB_{Z1}, CFB_{Z2}, CFB_{Z3}, and CFB_{Z4} (see Table 1), which differ only by their roughness length Z_{0b} values.

To assess the extent to which bottom drag damps the North Atlantic gyre and the GS, time-averaged barotropic vorticity budgets are estimated over the areas they cover. The barotropic vorticity budget is a classical diagnostic used to analyze the circulation of ocean gyres and the GS (see *e.g.,* Le Corre et al., 2020; Schoonover et al., 2016). Following Schoonover et al. (2016), for gyre identification we use closed barotropic streamfunction contours of −1 Sv (1 Sv = 10^6 m^3 s^{-1}), while for GS identification we use the closed barotropic streamfunction between 1 and 30 Sv with a southern edge at 28°N and an eastern edge at −60°N. As a whole, the North Atlantic Gyre (not shown) is not in a Sverdrup balance—between surface stress curl $\left(\frac{\nabla\times\tau}{\rho_0}\right)$ and planetary vorticity advection ($-\nabla.(f\mathbf{U})$). Instead, consistent with Schoonover et al. (2016), the anticyclonic vorticity provided by the surface stress curl is primarily balanced by the bottom pressure torque $\left(\frac{J(P_b,h)}{\rho_0}\right)$ and, to a lesser extent, by bottom drag $\left(-\frac{\nabla\times\tau_\mathbf{b}}{\rho_0}\right)$. On the GS (Figure 8), the dynamics are different and the main equilibrium in the CFB simulations is between the planetary vorticity advection ($-\nabla.(f\mathbf{U})$) and the bottom pressure torque $\left(\frac{J(P_b,h)}{\rho_0}\right)$. This can be interpreted as a balance between the inertial effect of the mean GS and its control by the topography. At the sharp curvature of Cape Hatteras, inertia overrides topographic control and separation can occur. This process is robust through the bottom roughness tests and the vorticity budget does not show much sensitivity, although the nonlinear torque ($\mathcal{A}$) becomes progressively larger as Z_{0b} decreases, partially replacing the bottom pressure torque.

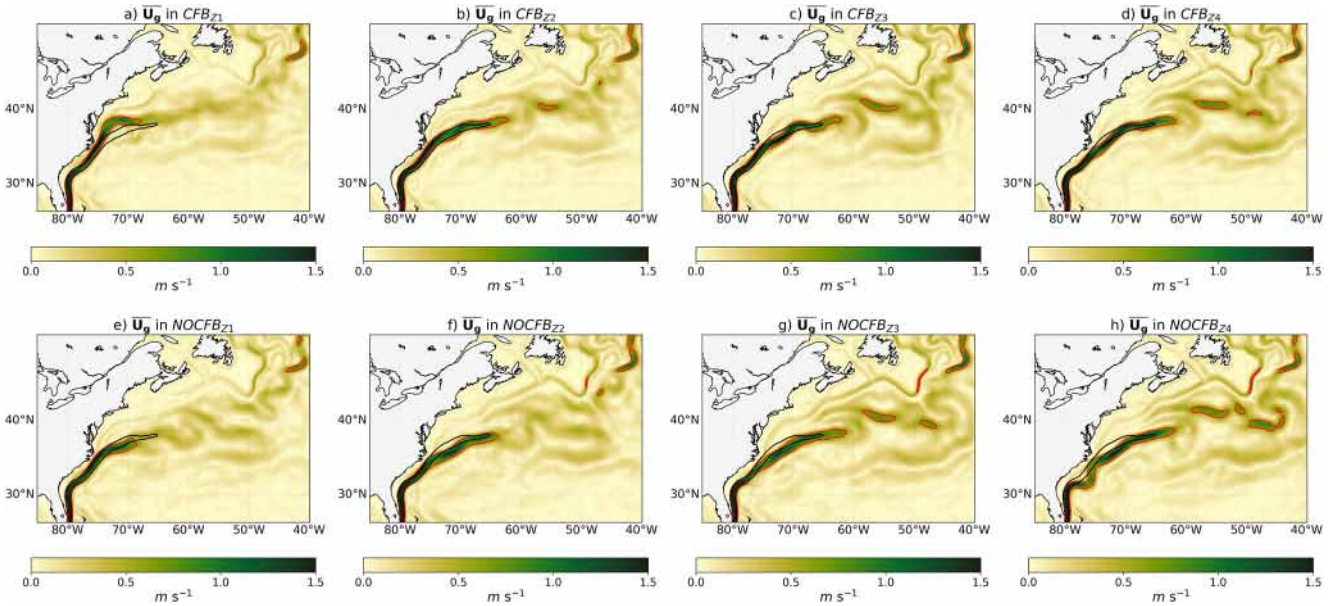

Figure 9. Top panel: mean surface geostrophic currents from CFB_{Z1} (a), CFB_{Z2} (b), CFB_{Z3} (c) and CFB_{Z4} (d). Bottom panel: same but for the *NOCFB* simulations. The red and black contours represent the mean path of the Gulf Stream identified using the contour of 0.6 m s^{-1} from the simulations and from the AVISO MDT, respectively.

The GS appears modulated to some extent by the magnitude of roughness length in CFB simulations (Figures 9 and 10a). The mean surface geostrophic currents are compared with estimations from AVISO altimetry (red and black contours delimiting the mean GS current). In CFB_{Z4}, a weak bottom friction induces two main biases: a premature separation (mean position around 34.8°N, Figure 3d) associated with a weak transport, and excessive post-separation transport — particularly on the North England Seamount, where transport is greater than 250 Sv. By gradually increasing Z_{0b}, the GS position becomes less premature and the transport is increased near Cape Hatteras and reduced over the North England Seamount. The impact of bottom friction can also be observed in *EKE* from CFB and NOCFB experiments (Figure 11). As Z_{0b} decreases, the *EKE* tends to increase in North England Seamounts and to decrease at Cape Hatteras. However, the most unrealistic GS behavior is seen at the other end of the roughness range, for CFB_{Z1}, with overshooting (separation at about 36.2°, Figure 3) and a weak post-separation transport (with a local maximum of ≈130 Sv over the North England Seamount).

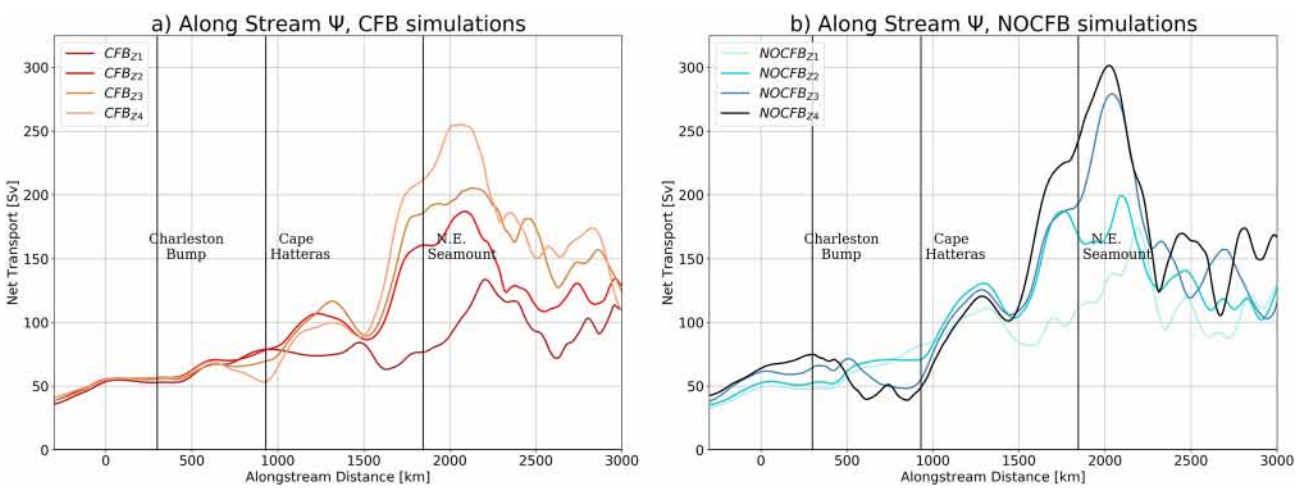

Figure 10. Alongstream Gulf Stream transport estimated from the current feedback simulations (a) and NOCFB simulations (b).

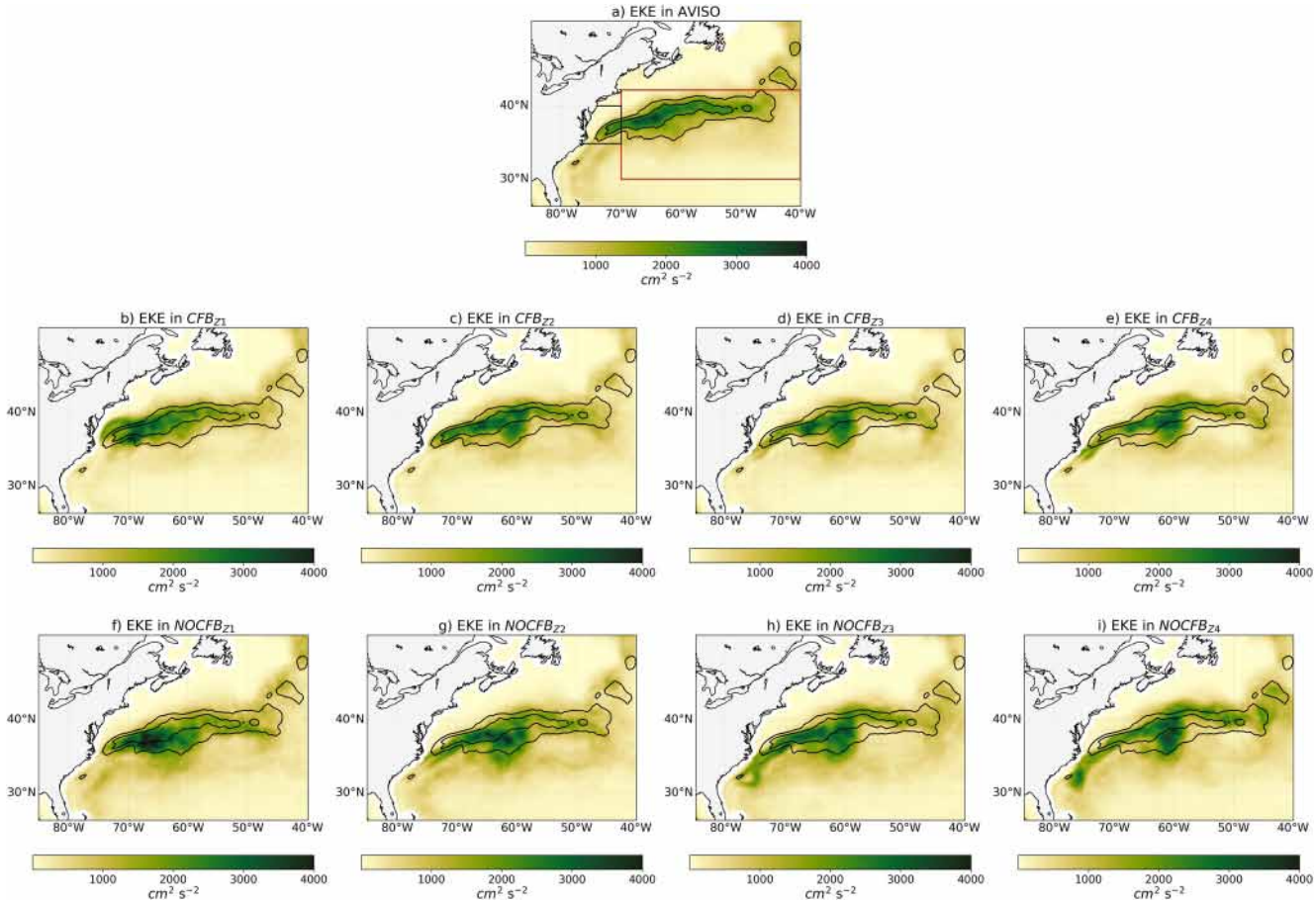

Figure 11. Same as Figure 5 but for AVISO (a), CFB_{Z1} (b), CFB_{Z2} (c), CFB_{Z3} (d), CFB_{Z4} (e), $NOCFB_{Z1}$ (f), $NOCFB_{Z2}$ (g), $NOCFB_{Z3}$ (h), $NOCFB_{Z4}$ (i).

As illustrated in Figures 11 and 5d, bottom roughness also has a moderate impact on EKE in GS separation and post-separation regimes. The stronger post-separation GS in CFB_{Z3} and CFB_{Z4} tends to amplify eddy advection, redistributing EKE along the GS path (larger differences between separation and post-separation EKE values, compared with CFB_{Z2} and AVISO; Figure 5d). Again, the largest sensitivity is on the other end of the range (CFB_{Z1}), where EKE is too strong near Cape Hatteras, likely because the offshore eddy advection by the GS is weak in this case (Figure 5d). Overall, and as expected, a larger Z_{0b} leads to more intense dissipation through bottom drag, a weaker GS, and an eddy advection. Finally, to summarize, among the CFB simulations, CFB_{Z2} gives the most realistic results.

4.2. Coaction of Top and Bottom Drags

Until very recently, top drag was generally ignored in simulations of ocean circulation and modelers relied instead on interior or bottom dissipation to remove the excessive energy present in eddy-rich models (Renault, Marchesiello, et al., 2019). Therefore, the role of these processes, particularly the bottom drag, may be overestimated. The main goal of this section is to assess the top drag mitigation of the bottom drag effect on the NATL circulation and GS characteristics.

All simulations with no CFB show an excess of energy that is reflected in the mean surface geostrophic currents (Figure 9) and mean EKE (Figure 11). Thus, they are all biased to varying degrees, although the simulation with high bottom roughness ($NOCFB_{Z1}$) now appears to be the most realistic, as its bottom dissipation seems to partly compensate for the lack of top drag. The mean GS path in $NOCFB_{Z1}$ is similar to that of the reference simulation with top drag (CFB_{Z2}) but with a more convex separation of around 35.6°N (Figure 3d). The alongstream GS transport is also similar to CFB_{Z2} near the GS separation but weaker over the North England Seamount

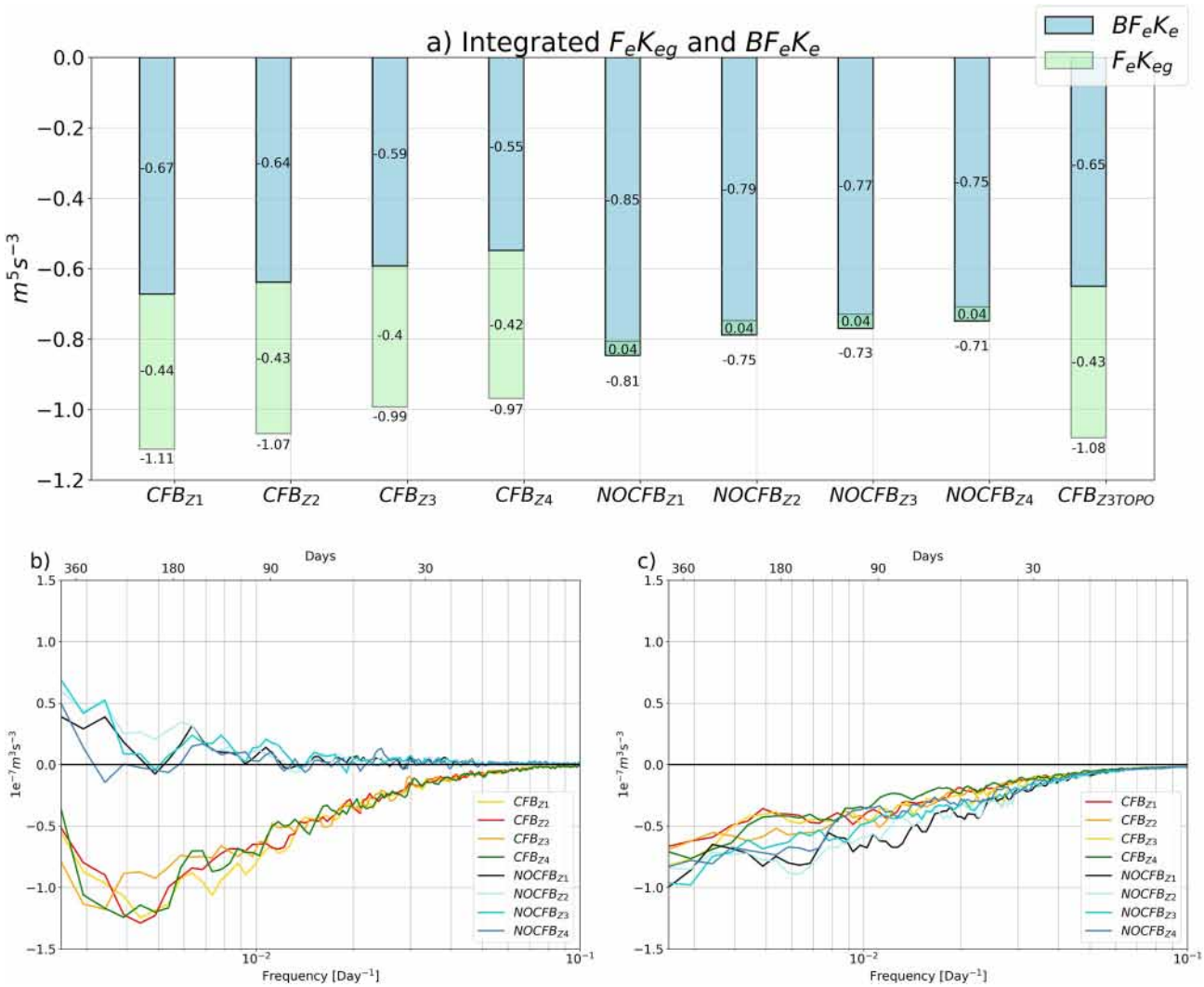

Figure 12. (a) F_eK_{eg} and BF_eK_e integrated over the domain shown in for example, Figure 5 for the current feedback and NOCFB simulations. Note the positive values of F_eK_{eg} that add up to the negative values of BF_eK_e. Integrated values are indicated inside the bars while their sum is specified below the bars. Frequency cospectra of the surface stress work Λ_{surf} (a) and bottom stress work Λ_b (b). At the mesoscale, current feedback causes a negative stress work that is only partly compensated for by excessive bottom roughness (roughly 30%) in the NOCFB simulations.

(Figure 10). However, at the mesoscale, the high bottom drag only partially replaces the top drag, as surface EKE levels remain excessive relative to observations, especially after separation (Figure 5d).

Simulations without top drag and with weak bottom drag reveal more significant problems. Both $NOCFB_{Z3}$ and $NOCFB_{Z4}$ are too energetic. The alongstream mean transport is largely impacted, as illustrated by a wide spread over the North England Seamount (between 130 Sv in $NOCFB_{Z1}$ and over 300 Sv in $NOCFB_{Z4}$). In $NOCFB_{Z3}$ and $NOCFB_{Z4}$, the GS has two additional biases. First, the separation of the GS is premature with a mean position around 34.6°N and 34.7°N (Figure 3). Second, especially in $NOCFB_{Z4}$, the EKE above the Charleston hump is too large due to intense instability — baroclinic conversion (P_eK_e) over the bump and barotropic conversion (K_mK_e) downstream (not shown) — resulting in residual meandering. Such strong sensitivity is absent from the *CFB* simulations.

The change of dynamics without top drag is also reflected in the mean barotropic vorticity budget (Figure 8). Both the North Atlantic Gyre (not shown) and the GS regions present a large sensitivity to bottom roughness. On the GS, the nonlinear torque has a positive contribution that becomes progressively larger to the point of supplanting the bottom pressure torque in $NOCFB_{Z4}$ with low bottom drag. We understand that a small amount

of dissipation in the absence of top drag and with low bottom drag allows nonlinear processes to dominate the dynamics of the GS, and the current is seen meandering and departing from the topographic slope, which cannot exercise much control. Therefore, a key difference with CFB simulations is the high sensitivity of NOCFB simulations to Z_{0b}, which has difficulty dissipating sufficient energy in the system.

Finally, F_eK_{eg} and BF_eK_e are integrated over the domain shown in for example, Figure 5, excluding shallow depth under 200 m for F_eK_{eg} to avoid positive values unrelated to the mesoscale activity. The result is shown in Figure 12, together with a co-spectral analysis of surface and bottom stress work over a region around the GS post-separation. The co-spectra are estimated as $\Lambda_{surf} = \mathrm{Re}\left(\hat{\boldsymbol{\tau}} \cdot \widehat{\mathbf{U_{og}}}^*\right)$ and $\Lambda_{bot} = \mathrm{Re}\left(\hat{\boldsymbol{\tau}}_{\boldsymbol{b}} \cdot \widehat{\mathbf{U_b}}^*\right)$, where $\hat{\boldsymbol{\tau}}$ and $\hat{\boldsymbol{\tau}}_{\boldsymbol{b}}$ are the Fourier transforms of the surface and bottom stress vectors, respectively; and $\widehat{\mathbf{U_{og}}}^*$ and $\widehat{\mathbf{U_b}}^*$ are the conjugates of the Fourier transform of the surface geostrophic current and bottom current vectors, respectively. Consistent with Renault, Molemaker, McWilliams, et al. (2016) and Jullien et al. (2020), the CFB simulations are characterized by a negative F_eK_{eg} and by a peak of negative surface stress work at mesoscale that reflects a transfer of energy from oceanic eddies to the atmosphere (the *eddy killing* process). This process is absent from the NOCFB simulations and the surface stress work has small positive values that become significant at time scales greater than 80 days — the usual large-scale wind forcing. The integrated F_eK_{eg} is therefore slightly positive in all NOCFB simulations. As expected, in both CFB and NOCFB simulations, the co-spectra of bottom stress work is negative, indicating energy dissipation through bottom friction. In the CFB simulations, dissipation by the bottom drag is greater than that by the top drag (about 60% and 40% of the total), and the greater the roughness, the more intense the bottom dissipation (the top drag is barely sensitive). In the NOCFB simulations, the bottom dissipation increases by about 30%, which only partially compensates for the lack of top drag. The cumulative surface and bottom dissipation in the CFB simulations is about 35% larger than the bottom dissipation alone in NOCFB, even though the bottom drag is probably overestimated in these simulations (at least in $NOCFB_{Z1}$).

5. A Simple Parametrization of Bottom Form Drag

In this section, we evaluate the effect of the subgrid topographic parameterization in CFB_{Z3TOPO} (see Section 2.2.1), comparing it to CFB_{Z2}, that is, the most realistic CFB simulation, and to CFB_{Z3} which shares the same Z_{0b}. The c_t factor applied to the bottom stress in CFB_{Z3TOPO} is illustrated in Figure 13a. Not surprisingly, c_t is larger near the shelves and where subgrid topography is not resolved by the model. Figure 13a–13d. shows the mean surface geostrophic currents and surface EKE from CFB_{Z3TOPO}, as well as a cross-section of summer currents at Cape Hatteras. The subgrid parametrization in CFB_{Z3TOPO} seems to correct most of the biases present in CFB_{Z3}, that is, too much mesoscale activity and premature GS separation (see Figure 3d). CFB_{Z3TOPO} is thus similar to CFB_{Z2}, considering surface currents (Figures 9b and 13b), EKE (Figures 5 and 13c) and alongstream GS transport (not shown). The cross-section near Cape Hatteras in Figure 13d also confirms a realistic GS intensity and position (compare with Figure 4).

The form drag estimated with the standard deviation of subgrid topography in CFB_{Z3TOPO} seems to refine the spatial distribution of eddy bottom stress work (BF_eK_e) compared to CFB_{Z2} (Figure 14). A similar result is found for the mean bottom stress work (BF_mK_m, not shown). As expected, the parameterization is most effective over regions with intense dynamics and where c_t is large. To better highlight the differences between CFB_{Z1}, CFB_{Z2}, CFB_{Z3}, and CFB_{Z3TOPO}, the probability density function of their mean bottom stress $\left(\overline{\tau_b}\right)$ is computed and shown in Figure 14b. Interestingly, for weak values of $\overline{\tau_b}$ (<0.0025 N m^{-2}), CFB_{Z3TOPO} resembles CFB_{Z1}. Then for values of $\overline{\tau_b} < 0.08$ N m^{-2}, CFB_{Z3TOPO} is closer to CFB_{Z2}, and for larger values, CFB_{Z3TOPO} is between CFB_{Z2} and CFB_{Z1}.

6. Conclusion

Using a set of North Atlantic oceanic simulations, we assess the role of top and bottom drags in driving GS dynamics and the extent to which top drag mediates the importance of bottom drag. In good agreement with former studies, we show that top drag (from the CFB effect) stabilizes the GS and partly controls its separation by inducing a sink of energy from oceanic eddies to the atmosphere (*eddy killing*). The sensitivity of ocean dynamics to bottom drag was more uncertain because all previous studies assessed it in the absence of top drag, that is, ocean-atmosphere coupling through CFB. Here, we revisit these studies with active top and bottom drags and can only confirm some of their results. For example, bottom friction can affect GS dynamics through dissipation of the mean and eddy flow and modification of eddy-mean interaction (barotropic and baroclinic energy conversions). However, we find that numerical solutions without top drag are overly sensitive to bottom drag coeffi-

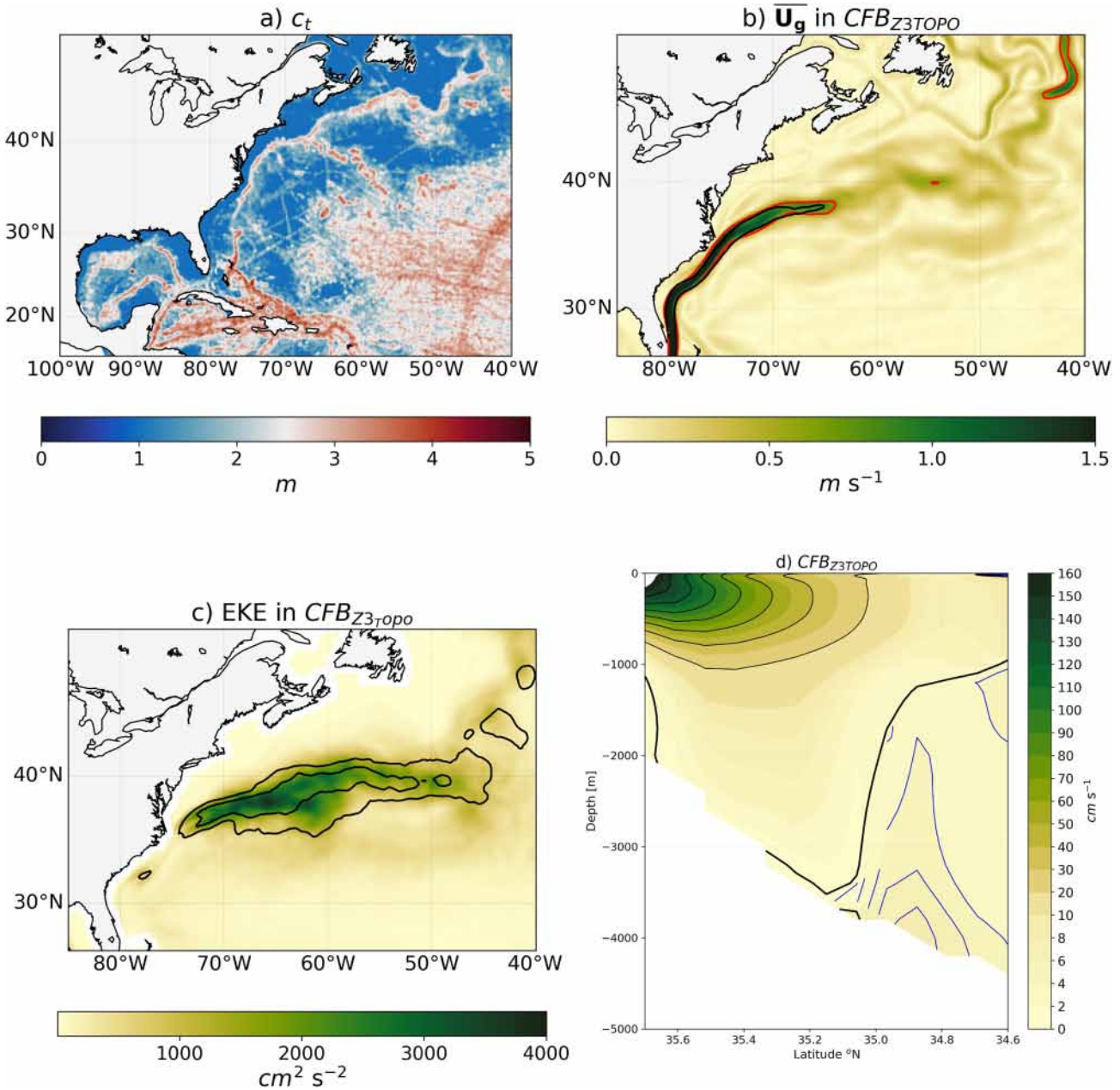

Figure 13. (a) The c_t corrective factor applied in the CFB_{Z3TOPO} experiment. (b) Mean surface geostrophic current from CFB_{Z3TOPO} zoomed over a region that encompasses the Gulf Stream. The red and black contours represent the mean path of the Gulf Stream identified using the contour of 0.6 m s^{-1} from the simulations and from AVISO, respectively. (c) same than (b) but for the surface geostrophic EKE (using smooth currents as in Figure 5). The black contours represent the EKE levels of 1,000 and 2,000 cm^{2}s^{-2} from AVISO; (d) Cross-section at Cape Hatteras of the mean geostrophic currents during summer. The subgrid parameterization of bottom form drag allows correcting most of the biases of the CFB_{Z3} simulation.

cients, indicating that CFB mitigates this sensitivity to a large extent. In an eddy-rich ocean simulation with no top drag, the lack of energy sink to the atmosphere is only partially compensated for by the bottom friction, even when overused, leading to an unstable system with too much energy. In this case, mean currents and mesoscale activity are controlled to a certain extent but through spurious processes.

In most oceanic models, bottom friction is parametrized using a constant drag coefficient or roughness length that is generally based on sensitivity study rather than physical arguments. As detailed in the introduction, at eddy-rich spatial resolution, the bottom drag is dominated by form drag or wave drag produced by subgrid-scale topography. In CROCO, a roughness length value of $z_{0b} = 10^{-2}$ m is often used because it allows a fair representa-

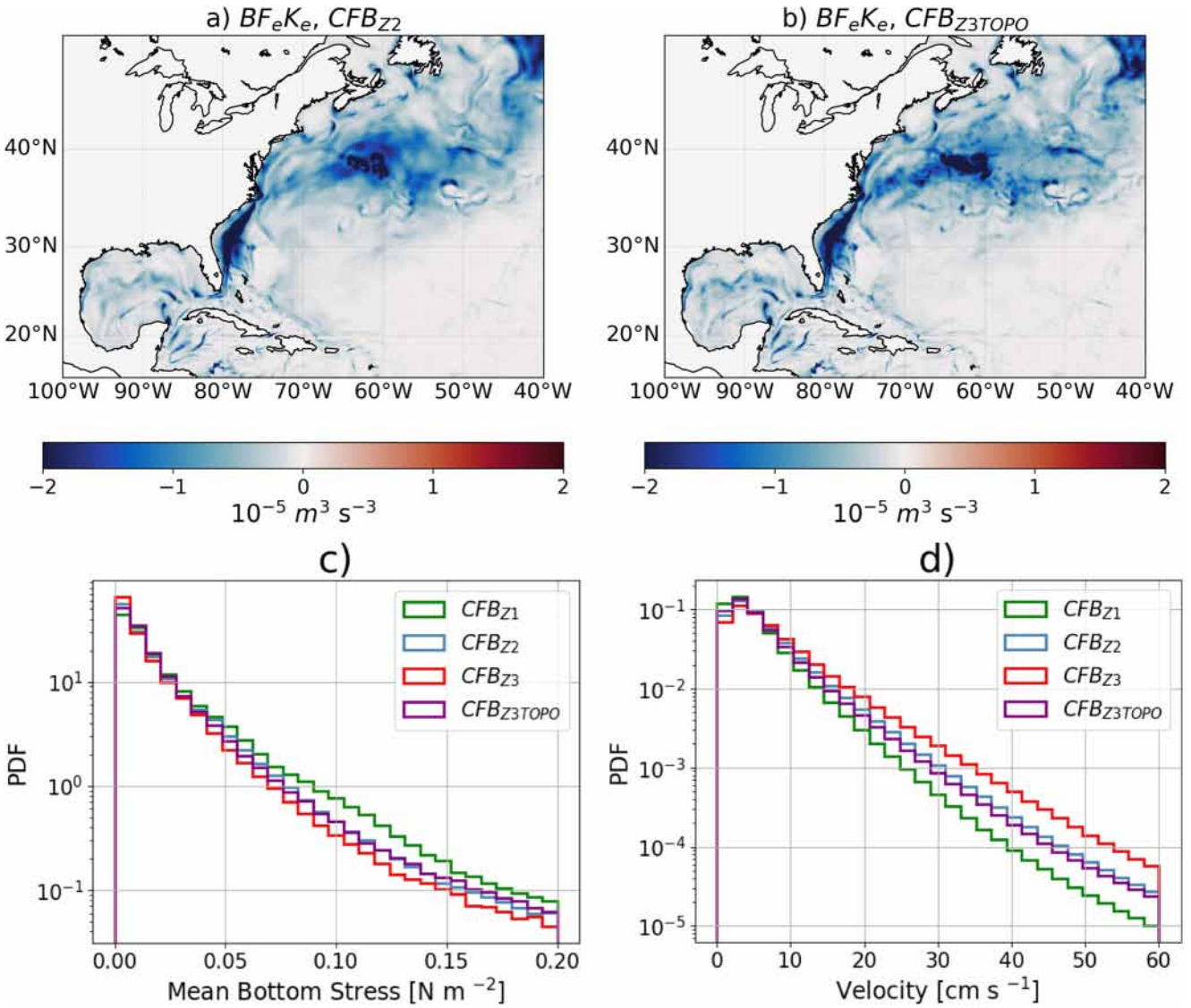

Figure 14. Top panel: Eddy bottom stress work (BF_eK_e) from CFB_{Z2} (a) and CFB_{Z3TOPO} (b). Bottom panel: Probability Density Function of the mean bottom stress (c) and bottom current (d).

tion of oceanic circulation at mesoscale resolutions (≈5 − 10 km). This value is much larger than sand-grain roughness and roughly accounts for subgrid-scale topographic effects. Based on previous studies from Belcher and Wood (1996); Jimenez and Dudhia (2012); Trossman et al. (2013, 2016), we developed and tested a simple parameterization. We assumed that the form/wave bottom drag is primarily associated with the magnitude of subgrid topographic variability, represented as a correction factor to a background frictional drag. In this case, a background roughness $z_{0b} = 10^{-3}$ m is enough to reproduce the main features of the GS, similar to simulations with larger z_{0b} (between 10^{-2} and 10^{-1} m). An advantage of this parametrization is that it is scale-aware, that is, resolution-dependent through the use of subgrid topography variance. Therefore, to fully appreciate its benefits for ocean models, it must be tested at a higher spatial resolution—reducing effective roughness—and over other regions of the world. This will be the focus of further research.

The reduced sensitivity to bottom drag when top drag is included is somewhat consistent with the reduced dissipation associated with bottom drag when wave drag is included in Trossman et al. (2016) or when the resolution of the bottom boundary layer is increased (Ruan et al., 2021). In our study, other missing processes are still uncertain. For example, submesoscale dynamics and associated air-sea coupling may play some role in the energy pathways of the GS system. Submesoscale ocean currents occur on an intermediate scale on the order

of 0.1–10 km horizontally, 10–100 m vertically, and hours to days temporally, that is, smaller and shorter than mesoscale currents, but large enough that rotation and density stratification are important. Our simulations are too coarse to represent them but submesoscale currents can affect momentum, buoyancy, and gas exchange between the ocean and atmosphere (Su et al., 2018). They can also impact the oceanic interior route to energy dissipation (Contreras et al., 2023; Gula et al., 2016; Schubert et al., 2020). In particular, they can drive a forward cascade of energy that is often represented in oceanic models by subgrid-scale turbulent viscosity (modeled as a combination of physical and numerical closure as in e.g., Chassignet & Xu, 2017). However, as shown by Klein et al. (2019) and Schubert et al. (2019), they also extend the range of the inverse energy cascade by energizing mesoscale currents. Although the magnitude of the interior ocean dissipation pathway remains an open question, in the boundary layers, the top and bottom drag represent efficient physical dissipation processes that still warrant better representation.

Some of the uncertainty may come from the wave interface, which is never explicitly included in basin-scale simulations. The sea-state may directly modulate the dissipation by top drag by altering the roughness of the ocean. Tidal effects on bottom friction are also often neglected, although they could also modulate the top drag effect. Müller et al. (2010) show that bottom friction and mixing can be significantly modified by tides and their nonlinear interaction with low frequency motions. To assess the extent to which tides can affect GS dynamics, we performed a simulation with tidal forcing, top drag from CFB, and bottom drag with coefficients modulated by subgrid topography. At open boundaries, tidal data (elevation and barotropic currents) were derived from the Oregon State University global models of ocean tides TPXO7 (Egbert & Erofeeva, 2002), and applied through Flather-type conditions as for other barotropic currents. Because the computational domain covers a large basin, the tidal potential was also applied as a body force in the interior. In this simulation, consistent with Müller et al. (2010), we find that the main tidal impact occurs in the Subpolar Gyre, but GS dynamics are not significantly different from simulations without tidal forcing.

In conclusion, our results may have significant implications for the understanding of GS dynamics. The top drag from mesoscale air-sea interaction appears to be essential. The bottom drag must be calibrated or parameterized appropriately, but its importance is diminished by the top drag. To refine our conclusions, additional surface, and deep oceanic observations would be needed. Future satellite missions such as Odysea (Bourassa et al., 2016; Rodríguez et al., 2018) aim to measure surface currents and surface stress in a consistent manner. This would provide a better understanding of the surface stress response to CFB, the resulting wind work, and associated eddy killing. In addition, this could also allow us to derive coupling coefficients between the surface current, surface stress, and overlying wind, which could then be used in the CFB parameterization.

Data Availability Statement

Data can be downloaded from https://figshare.com/s/d91f5e638d654e765ed5.

Acknowledgments
We appreciate the support from the GdR and GdRI CROCO, ANR-JPOC EUREC4A-OA, CNRS-INSU LEFE VENUS, and CNES TOSCA I-CASCADE, CARAMBA, and M_oDYSEA projects. This work used the GENCI #A0050107298 and #A005013051 computing resources. L.R. thanks M.C.R and J.R.C. for useful discussions.

References

Arbic, B. K., Shriver, J. F., Hogan, P. J., Hurlburt, H. E., McClean, J. L., Metzger, E. J., et al. (2009). Estimates of bottom flows and bottom boundary layer dissipation of the oceanic general circulation from global high-resolution models. *Journal of Geophysical Research*, *114*(C2), C02024. https://doi.org/10.1029/2008jc005072

Belcher, S. E., & Wood, N. (1996). Form and wave drag due to stably stratified turbulent flow over low ridges. *Quarterly Journal of the Royal Meteorological Society*, *122*(532), 863–902. https://doi.org/10.1002/qj.49712253205

Bourassa, M. A., Rodriguez, E., & Chelton, D. (2016). Winds and currents mission: Ability to observe mesoscale air/sea coupling. In *Geoscience and Remote sensing Symposium (IGARSS), 2016 IEEE international* (pp. 7392–7395). IEEE.

Bryan, F. O., Böning, C. W., & Holland, W. R. (1995). On the midlatitude circulation in a high-resolution model of the north atlantic. *Journal of Physical Oceanography*, *25*(3), 289–305. https://doi.org/10.1175/1520-0485(1995)025<0289:otmcia>2.0.co;2

Bryan, F. O., Hecht, M. W., & Smith, R. D. (2007). Resolution convergence and sensitivity studies with north atlantic circulation models. part i: The Western boundary current system. *Ocean Modelling*, *16*(3), 141–159. https://doi.org/10.1016/j.ocemod.2006.08.005

Bye, J. A. (1985). *Large-scale momentum exchange in the coupled atmosphere-ocean* (Vol. 40, pp. 51–61). Elsevier oceanography series.

Carton, J. A., & Giese, B. S. (2008). A reanalysis of ocean climate using simple ocean data assimilation (SODA). *Monthly Weather Review*, *136*(8), 2999–3017. https://doi.org/10.1175/2007mwr1978.1

Chassignet, E. P., & Marshall, D. P. (2008). Gulf stream separation in numerical ocean models. *Ocean Modeling in an Eddying Regime*, 39–61. https://doi.org/10.1029/177gm05

Chassignet, E. P., Smith, L. T., Halliwell, G. R., & Bleck, R. (2003). North atlantic simulations with the hybrid coordinate ocean model (hycom): Impact of the vertical coordinate choice, reference pressure, and thermobaricity. *Journal of Physical Oceanography*, *33*(12), 2504–2526. https://doi.org/10.1175/1520-0485(2003)033<2504:naswth>2.0.co;2

Chassignet, E. P., & Xu, X. (2017). Impact of horizontal resolution (1/12 to 1/50) on gulf stream separation, penetration, and variability. *Journal of Physical Oceanography*, *47*(8), 1999–2021. https://doi.org/10.1175/jpo-d-17-0031.1

Chelton, D. B., Schlax, M. G., & Samelson, R. M. (2011). Global observations of nonlinear mesoscale eddies. *Progress in Oceanography*, *91*(2), 167–216. https://doi.org/10.1016/j.pocean.2011.01.002

Contreras, M., Renault, L., & Marchesiello, P. (2023). Understanding energy pathways in the Gulf Stream. *Journal of Physical Oceanography*, *53*, 719–736. https://doi.org/10.1175/JPO-D-22-0146.1

Couvelard, X., Marchesiello, P., Gourdeau, L., & Lefèvre, J. (2008). Barotropic zonal jets induced by islands in the southwest Pacific. *Journal of Physical Oceanography*, *38*(10), 2185–2204. https://doi.org/10.1175/2008jpo3903.1

Debreu, L., Kevlahan, N., & Marchesiello, P. (2022). Improved Gulf Stream separation through Brinkman penalization. *Ocean Modelling*, *179*, 102121. https://doi.org/10.1016/j.ocemod.2022.102121

Debreu, L., Marchesiello, P., Penven, P., & Cambon, G. (2012). Two-way nesting in split-explicit ocean models: Algorithms, implementation and validation. *Ocean Modelling*, *49*, 1–21. https://doi.org/10.1016/j.ocemod.2012.03.003

de Marez, C., Ahaye, N. J., & Gula, J. (2020). Interaction of the Gulf Stream with small scale topography: A focus on lee waves. *Scientific report*, *10*, 2332.

Dewar, W. K., & Flierl, G. R. (1987). Some effects of the wind on rings. *Journal of Physical Oceanography*, *17*(10), 1653–1667. https://doi.org/10.1175/1520-0485(1987)017<1653:seotwo>2.0.co;2

Duhaut, T. H., & Straub, D. N. (2006). Wind stress dependence on ocean surface velocity: Implications for mechanical energy input to ocean circulation. *Journal of Physical Oceanography*, *36*(2), 202–211. https://doi.org/10.1175/jpo2842.1

Egbert, G. D., & Erofeeva, S. Y. (2002). Efficient inverse modeling of barotropic ocean tides. *Journal of Atmospheric and Oceanic Technology*, *19*(2), 183–204. https://doi.org/10.1175/1520-0426(2002)019<0183:eimobo>2.0.co;2

Fairall, C., Bradley, E. F., Hare, J., Grachev, A., & Edson, J. (2003). Bulk parameterization of air-sea fluxes: Updates and verification for the coare algorithm. *Journal of Climate*, *16*(4), 571–591. https://doi.org/10.1175/1520-0442(2003)016<0571:bpoasf>2.0.co;2

Gula, J., Molemaker, M. J., & McWilliams, J. C. (2015). Gulf stream dynamics along the southeastern us seaboard. *Journal of Physical Oceanography*, *45*(3), 690–715. https://doi.org/10.1175/jpo-d-14-0154.1

Gula, J., Molemaker, M. J., & McWilliams, J. C. (2016). Topographic generation of submesoscale centrifugal instability and energy dissipation. *Nature Communications*, *7*(1), 12811. https://doi.org/10.1038/ncomms12811

Hurlburt, H. E., & Hogan, P. J. (2008). The gulf stream pathway and the impacts of the eddy-driven abyssal circulation and the deep Western boundary current. *Dynamics of Atmospheres and Oceans*, *45*(3–4), 71–101. https://doi.org/10.1016/j.dynatmoce.2008.06.002

Jimenez, P. A., & Dudhia, J. (2012). Improving the representation of resolved and unresolved topographic effects on surface wind in the WRF model. *Journal of Applied Meteorology and Climatology*, *51*(2), 300–316. https://doi.org/10.1175/jamc-d-11-084.1

Johns, W. E., Shay, T., Bane, J., & Watts, D. (1995). Gulf stream structure, transport, and recirculation near 68 w. *Journal of Geophysical Research*, *100*(C1), 817–838. https://doi.org/10.1029/94jc02497

Jullien, S., Masson, S., Oerder, V., Samson, G., Colas, F., & Renault, L. (2020). Impact of ocean-atmosphere current feedback on the ocean mesoscale activity: Regional variations, and sensitivity to model resolution. *Journal of Climate*, *33*(7), 2585–2602. https://doi.org/10.1175/jcli-d-19-0484.1

Klein, P., Lapeyre, G., Siegelman, L., Qiu, B., Fu, L.-L., Torres, H., et al. (2019). Ocean-scale interactions from space. *Earth and Space Science*, *6*(5), 795–817. https://doi.org/10.1029/2018ea000492

Klymak, J. M. (2018). Nonpropagating form drag and turbulence due to stratified flow over large-scale abyssal Hill topography. *Journal of Physical Oceanography*, *48*(10), 2383–2395. https://doi.org/10.1175/jpo-d-17-0225.1

Large, W. G., McWilliams, J. C., & Doney, S. C. (1994). Oceanic vertical mixing: A review and a model with a nonlocal boundary layer parameterization. *Reviews of Geophysics*, *32*(4), 363–404. https://doi.org/10.1029/94rg01872

Larrañaga, M., Renault, L., & Jouanno, J. (2022). Partial control of the loop current dynamics by mechanical air-sea coupling. *Journal of Physical Oceanography*, *52*(10), 2515–2530. https://doi.org/10.1175/jpo-d-21-0271.1

Le Corre, M., Gula, J., & Tréguier, A.-M. (2020). Barotropic vorticity balance of the north atlantic subpolar gyre in an eddy-resolving model. *Ocean Science*, *16*(2), 451–468. https://doi.org/10.5194/os-16-451-2020

Lemarié, F. (2015). *Numerical modification of atmospheric models to include the feedback of oceanic currents on air-sea fluxes in ocean-atmosphere coupled models, Technical Report RT-464*, INRIA Grenoble - Rhône-Alpes; Laboratoire Jean Kuntzmann; Universite de Grenoble I - Joseph Fourier. INRIA.

Lemarié, F., Kurian, J., Shchepetkin, A. F., Molemaker, M. J., Colas, F., & McWilliams, J. C. (2012). Are there inescapable issues prohibiting the use of terrain-following coordinates in climate models? *Ocean Modelling*, *42*, 57–79. https://doi.org/10.1016/j.ocemod.2011.11.007

Ma, X., Jing, Z., Chang, P., Liu, X., Montuoro, R., Small, R. J., et al. (2016). Western boundary currents regulated by interaction between ocean eddies and the atmosphere. *Nature*, *535*(7613), 533–537. https://doi.org/10.1038/nature18640

Marchesiello, P., Debreu, L., & Couvelard, X. (2009). Spurious diapycnal mixing in terrain-following coordinate models: The problem and a solution. *Ocean Modelling*, *46*(3–4), 156–169. https://doi.org/10.1016/j.ocemod.2008.09.004

Marchesiello, P., McWilliams, J. C., & Shchepetkin, A. (2001). Open boundary conditions for long-term integration of regional oceanic models. *Ocean Modelling*, *3*(1), 1–20. https://doi.org/10.1016/s1463-5003(00)00013-5

Marchesiello, P., McWilliams, J. C., & Shchepetkin, A. (2003). Equilibrium structure and dynamics of the California current system. *Journal of Physical Oceanography*, *33*(4), 753–783. https://doi.org/10.1175/1520-0485(2003)33<753:esadot>2.0.co;2

McWilliams, J. C. (2008). The nature and consequences of oceanic eddies. *Ocean Modeling in an Eddying Regime*, 5–15. https://doi.org/10.1029/177gm03

Müller, M., Haak, H., Jungclaus, J., Sündermann, J., & Thomas, M. (2010). The effect of ocean tides on a climate model simulation. *Ocean Modelling*, *35*(4), 304–313. https://doi.org/10.1016/j.ocemod.2010.09.001

Oerder, V., Colas, F., Echevin, V., Masson, S., Hourdin, C., Jullien, S., et al. (2016). Mesoscale sst–wind stress coupling in the Peru–Chile current system: Which mechanisms drive its seasonal variability? *Climate Dynamics*, *47*(7–8), 2309–2330. https://doi.org/10.1007/s00382-015-2965-7

Özgökmen, T. M., & Chassignet, E. P. (2002). Dynamics of two-dimensional turbulent bottom gravity currents. *Journal of Physical Oceanography*, *32*(5), 1460–1478. https://doi.org/10.1175/1520-0485(2002)032<1460:dotdtb>2.0.co;2

Pickart, R. S., & Smethie, J. W. M. (1993). How does the deep Western boundary current cross the gulf stream? *Journal of Physical Oceanography*, *23*(12), 2602–2616. https://doi.org/10.1175/1520-0485(1993)023<2602:hdtdwb>2.0.co;2

Renault, L., Arsouze, T., & Ballabrera-Poy, J. (2021). On the influence of the current feedback to the atmosphere on the Western mediterranean sea dynamics. *Journal of Geophysical Research: Oceans*, *126*(1), e2020JC016664. https://doi.org/10.1029/2020jc016664

Renault, L., Lemarié, F., & Arsouze, T. (2019). On the implementation and consequences of the oceanic currents feedback in ocean–atmosphere coupled models. *Ocean Modelling*, *141*, 101423. https://doi.org/10.1016/j.ocemod.2019.101423

Renault, L., Marchesiello, P., Masson, S., & McWilliams, J. C. (2019). Remarkable control of Western boundary currents by eddy killing, a mechanical air-sea coupling process. *Geophysical Research Letters*, *46*(5), 2743–2751. https://doi.org/10.1029/2018gl081211

Renault, L., Masson, S., Arsouze, T., Madec, G., & McWilliams, J. C. (2020). Recipes for how to force oceanic model dynamics. *Journal of Advances in Modeling Earth Systems*, *12*(2), e2019MS001715. https://doi.org/10.1029/2019ms001715

Renault, L., McWilliams, J. C., & Gula, J. (2018). Dampening of submesoscale currents by air-sea stress coupling in the californian upwelling system. *Scientific Reports*, *8*(1), 13388. https://doi.org/10.1038/s41598-018-31602-3

Renault, L., McWilliams, J. C., Kessouri, F., Jousse, A., Frenzel, H., Chen, R., & Deutsch, C. (2021). Evaluation of high-resolution atmospheric and oceanic simulations of the California current system. *Progress in Oceanography*, *195*, 102564. https://doi.org/10.1016/j.pocean.2021.102564

Renault, L., McWilliams, J. C., & Masson, S. (2017). Satellite observations of imprint of oceanic current on wind stress by air-sea coupling. *Scientific Reports*, *7*(1), 17747. https://doi.org/10.1038/s41598-017-17939-1

Renault, L., McWilliams, J. C., & Penven, P. (2017). Modulation of the agulhas current retroflection and leakage by oceanic current interaction with the atmosphere in coupled simulations. *Journal of Physical Oceanography*, *47*(8), 2077–2100. https://doi.org/10.1175/jpo-d-16-0168.1

Renault, L., Molemaker, M. J., Gula, J., Masson, S., & McWilliams, J. C. (2016). Control and stabilization of the gulf stream by oceanic current interaction with the atmosphere. *Journal of Physical Oceanography*, *46*(11), 3439–3453. https://doi.org/10.1175/jpo-d-16-0115.1

Renault, L., Molemaker, M. J., McWilliams, J. C., Shchepetkin, A. F., Lemarié, F., Chelton, D., et al. (2016). Modulation of wind work by oceanic current interaction with the atmosphere. *Journal of Physical Oceanography*, *46*(6), 1685–1704. https://doi.org/10.1175/jpo-d-15-0232.1

Richardson, P. (1985). Average velocity and transport of the gulf stream near 55w. *Journal of Marine Research*, *43*(1), 83–111. https://doi.org/10.1357/002224085788437343

Rio, M.-H., Mulet, S., & Picot, N. (2014). Beyond goce for the ocean circulation estimate: Synergetic use of altimetry, gravimetry, and in situ data provides new insight into geostrophic and ekman currents. *Geophysical Research Letters*, *41*(24), 8918–8925. https://doi.org/10.1002/2014gl061773

Rodríguez, E., Wineteer, A., Perkovic-Martin, D., Gál, T., Stiles, B. W., Niamsuwan, N., & Monje, R. R. (2018). Estimating ocean vector winds and currents using a ka-band pencil-beam Doppler scatterometer. *Remote Sensing*, *10*(4), 576. https://doi.org/10.3390/rs10040576

Rooth, C., & Xie, L. (1992). Air-sea boundary layer dynamics in the presence of mesoscale surface currents. *Journal of Geophysical Research*, *97*(C9), 14431–14438. https://doi.org/10.1029/92jc01296

Ruan, X., Wenegrat, J. O., & Gula, J. (2021). Slippery bottom boundary layers: The loss of energy from the general circulation by bottom drag. *Geophysical Research Letters*, *48*(19), e2021GL094434. https://doi.org/10.1029/2021gl094434

Saha, S., Moorthi, S., Pan, H.-L., Wu, X., Wang, J., Nadiga, S., et al. (2010). The NCEP climate forecast system reanalysis. *Bulletin of the American Meteorological Society*, *91*(8), 1015–1057. https://doi.org/10.1175/2010bams3001.1

Sandwell, D. T., & Smith, W. H. (1997). Marine gravity anomaly from Geosat and ERS 1 satellite altimetry. *Journal of Geophysical Research: Solid Earth (1978–2012)*, *102*(B5), 10039–10054. https://doi.org/10.1029/96jb03223

Schoonover, J., Dewar, W. K., Wienders, N., & Deremble, B. (2017). Local sensitivities of the gulf stream separation. *Journal of Physical Oceanography*, *47*(2), 353–373. https://doi.org/10.1175/jpo-d-16-0195.1

Schoonover, J., Dewar, W., Wienders, N., Gula, J., McWilliams, J. C., Molemaker, M. J., et al. (2016). North atlantic barotropic vorticity balances in numerical models. *Journal of Physical Oceanography*, *46*(1), 289–303. https://doi.org/10.1175/jpo-d-15-0133.1

Schubert, R., Gula, J., Greatbatch, R. J., Baschek, B., & Biastoch, A. (2020). The submesoscale kinetic energy cascade: Mesoscale absorption of submesoscale mixed layer eddies and frontal downscale fluxes. *Journal of Physical Oceanography*, *50*(9), 2573–2589. https://doi.org/10.1175/jpo-d-19-0311.1

Schubert, R., Schwarzkopf, F. U., Baschek, B., & Biastoch, A. (2019). Submesoscale impacts on mesoscale agulhas dynamics. *Journal of Advances in Modeling Earth Systems*, *11*(8), 2745–2767. https://doi.org/10.1029/2019ms001724

Scott, R. B., & Xu, Y. (2009). An update on the wind power input to the surface geostrophic flow of the world ocean. *Deep Sea Research Part I: Oceanographic Research Papers*, *56*(3), 295–304. https://doi.org/10.1016/j.dsr.2008.09.010

Sen, A., Scott, R. B., & Arbic, B. K. (2008). Global energy dissipation rate of deep-ocean low-frequency flows by quadratic bottom boundary layer drag: Computations from current-meter data. *Geophysical Research Letters*, *35*(9), L09606. https://doi.org/10.1029/2008gl033407

Seo, H. (2017). Distinct influence of air–sea interactions mediated by mesoscale sea surface temperature and surface current in the arabian sea. *Journal of Climate*, *30*(20), 8061–8080. https://doi.org/10.1175/jcli-d-16-0834.1

Seo, H., Miller, A. J., & Norris, J. R. (2016). Eddy–wind interaction in the California current system: Dynamics and impacts. *Journal of Physical Oceanography*, *46*(2), 439–459. https://doi.org/10.1175/jpo-d-15-0086.1

Shchepetkin, A. F., & McWilliams, J. C. (2003). A method for computing horizontal pressure gradient force in an ocean model with a non-aligned vertical coordinate. *Journal of Geophysical Research*, *108*(C3), 3090. https://doi.org/10.1029/2001jc001047

Shchepetkin, A. F., & McWilliams, J. C. (2005). The regional oceanic modeling system (ROMS): A split-explicit, free-surface, topography-following-coordinate oceanic model. *Ocean Modelling*, *9*(4), 347–404. https://doi.org/10.1016/j.ocemod.2004.08.002

Shchepetkin, A. F., & McWilliams, J. C. (2009). Correction and commentary for ocean forecasting in terrain-following coordinates: Formulation and skill assessment of the regional ocean modeling system by Haidvogel et al., j. comp. phys. 227, pp. 3595–3624. *Journal of Computational Physics*, *228*(24), 8985–9000. https://doi.org/10.1016/j.jcp.2009.09.002

Soufflet, Y., Marchesiello, P., Lemarié, F., Jouanno, J., Capet, X., Debreu, L., & Benshila, R. (2016). On effective resolution in ocean models. *Ocean Modelling*, *98*, 36–50. https://doi.org/10.1016/j.ocemod.2015.12.004

Spall, M. A. (1996). Dynamics of the gulf stream/deep Western boundary current crossover. part i: Entrainment and recirculation. *Journal of Physical Oceanography*, *26*(10), 2152–2168. https://doi.org/10.1175/1520-0485(1996)026<2152:dotgsw>2.0.co;2

Stern, M. E. (1975). *Ocean circulation physics*. Academic Press, Inc.

Stern, M. E. (1998). Separation of a density current from the bottom of a continental slope. *Journal of Physical Oceanography*, *28*(10), 2040–2049. https://doi.org/10.1175/1520-0485(1998)028<2040:soadcf>2.0.co;2

von Storch, J.-S., Sasaki, H., & Marotzke, J. (2007). Wind-generated power input to the deep ocean: An estimate using a 1/10 general circulation model. *Journal of Physical Oceanography*, *37*(3), 657–672. https://doi.org/10.1175/jpo3001.1

Su, Z., Wang, J., Klein, P., Thompson, A. F., & Menemenlis, D. (2018). Ocean submesoscales as a key component of the global heat budget. *Nature Communications*, *9*(1), 1–8. https://doi.org/10.1038/s41467-018-02983-w

Thompson, J. D., & Schmitz, W., Jr. (1989). A limited-area model of the gulf stream: Design, initial experiments, and model-data intercomparison. *Journal of Physical Oceanography*, *19*(6), 791–814. https://doi.org/10.1175/1520-0485(1989)019<0791:alamot>2.0.co;2

Thoppil, P. G., Richman, J. G., & Hogan, P. J. (2011). Energetics of a global ocean circulation model compared to observations. *Geophysical Research Letters*, *38*(15). https://doi.org/10.1029/2011gl048347

Trossman, D. S., Arbic, B. K., Garner, S. T., Goff, J. A., Jayne, S. R., Metzger, E. J., & Wallcraft, A. J. (2013). Impact of parameterized lee wave drag on the energy budget of an eddying global ocean model. *Ocean Modelling*, *72*, 119–142. https://doi.org/10.1016/j.ocemod.2013.08.006

Trossman, D. S., Arbic, B. K., Richman, J. G., Garner, S. T., Jayne, S. R., & Wallcraft, A. J. (2016). Impact of topographic internal lee wave drag on an eddying global ocean model. *Ocean Modelling*, *97*, 109–128. https://doi.org/10.1016/j.ocemod.2015.10.013

Trossman, D. S., Arbic, B. K., Straub, D. N., Richman, J. G., Chassignet, E. P., Wallcraft, A. J., & Xu, X. (2017). The role of rough topography in mediating impacts of bottom drag in eddying ocean circulation models. *Journal of Physical Oceanography*, *47*(8), 1941–1959. https://doi.org/10.1175/jpo-d-16-0229.1

Wunsch, C. (1998). The work done by the wind on the oceanic general circulation. *Journal of Physical Oceanography*, *28*(11), 2332–2340. https://doi.org/10.1175/1520-0485(1998)028<2332:twdbtw>2.0.co;2

Xie, L., Liu, X., & Pietrafesa, L. J. (2007). Effect of bathymetric curvature on gulf stream instability in the vicinity of the charleston bump. *Journal of Physical Oceanography*, *37*(3), 452–475. https://doi.org/10.1175/jpo2995.1

Zhang, R., & Vallis, G. K. (2007). The role of bottom vortex stretching on the path of the north atlantic Western boundary current and on the northern recirculation gyre. *Journal of Physical Oceanography*, *37*(8), 2053–2080. https://doi.org/10.1175/jpo3102.1